To the Graduate Council:

I am submitting herewith a thesis written by John M. Lewis Jr. entitled "Normally Deformed States in ^{191}Tl." I have examined the final copy of this thesis for form and content and recommend that it be accepted in partial fulfillment of the requirements for the degree of Master of Science, with a major in Physics.

Lee L. Riedinger

Dr. L. L. Riedinger, Major Professor

We have read this thesis
and recommend its acceptance:

M W Guidry

Carrol Bingham

Accepted for the Council:

C W Minkel

Associate Vice Chancellor
and Dean of the Graduate School

Normally Deformed States in ^{191}Tl

A Thesis
Presented for the
Master of Science
Degree
The University of Tennessee, Knoxville

John M. Lewis Jr.
August 1994

ACKNOWLEDGEMENTS

I would like to thank the Nuclear Physics group for their support and encouragement along the way to the completion of this thesis. A special thanks goes to the members of my committiee, Dr. C. R. Bingham and Dr. M. W. Guidry for taking the time to read my work carefully and offer helpful suggestions. Sincere gratitude goes to my thesis advisor, Dr. L. L. Riedinger, for helping me each step of the way, not only with facts, but also with much encourgement and understanding. Dr. Riedinger has also alowed me the opportunity to explore avenues other than those related to the research and thus become more well-rounded person.

Secondly, I wish to thank all the post doctoral research associates that have been a resource to me over the last five years. It was Dr. S. Pilotte who helped me in the initial phase of the analysis, as well as teaching me about the experimental side, and being a very good friend. Dr. C.H. Yu was also instrumental in the early stages, by answering questions and helping me to develop an analytical approach. In the final stages of this work, Dr. W. Reviol helped me to solve some of the problem cases in the analysis. Sincere thanks go to him for his tireless assistance in the developing and polishing of this thesis. Thanks also go to Dr. R. W. Kincaid for his every ready help with the many questions that arose about the technical aspects of writing and finalizing the thesis.

Thirdly, thanks go out to those other students and staff members who have been a source of information and friendship. Thanks to W. Mueller and Dr. B. E. Zimmerman for helping with technical computing issues and for being a sounding board for both academic and personal issues. A special thanks goes to Dr. C. Baktash as he was my first contact with experimental nuclear physics and in the subsequent years was always willing to answer questions and offer help. Thanks should also go to the support people at the Oak Ridge National Laboratory, especially to C. Thomas, the computing system manager for always being helpful even for simple questions, and to M. Whitley for teaching me specifics about the detector arrays.

Finally I would like to thank my parents for their help and support both emotionally and financially throughout the course of this work. They, along with God's help and a special support group of friends outside the research group, offered the encouragement, diversion and love that have upheld me through all stages of this work.

This dissertation
is
dedicated
to my parents,
Mr. and Mrs. John M. Lewis

ABSTRACT

High-spin states of the ^{191}Tl nucleus were studied at the Oak Ridge Holified Heavy-Ion Research Facility and at the Argonne ATLAS Facility. In these experiments the heavy-ion fusion reactions ^{169}Tm(^{26}Mg,4n) and ^{159}Tb(^{36}S,4n) were used. The γ-ray spectroscopy data from these experiments were used to search for superdeformation, which is reported in another work, as well as to probe the normally deformed states of ^{191}Tl.

A variety of nuclear shapes were deduced from the data. Oblate rotational bands were seen built on both the $\pi h_{9/2}$ and $\pi i_{13/2}$ states. This was the first observation of an oblate $i_{13/2}$ rotational band. Other non-rotational structures were observed which seem to be more shperical in nature. And, the same data led to the establishment of superdeformed bands in this nucleus. Results from Total Routhian Surface calulations support these findings.

This work has significantly extended previous studies, adding 70 transitions to the level scheme. Intensities and DCO ratios have been extracted for each of these transitions and those previously known. The postive and negative parity rotational bands have been extended to spins of $\frac{45}{2}^+$ and $\frac{37}{2}^-$, respectively, enabling a study of the $(\nu i_{13/2})^2$ crossing frequencies in each band.

Contents

List of Figures

CHAPTER 1

Introduction

The purpose of this work is to study the nuclear structure of ^{191}Tl in order to learn about the surprising variety of nuclear shapes and level structures that can exist adjacent to a closed shell. With 81 protons, thallium is one proton short of a major closed shell which generally leads to spherical shapes at or near the ground state. This thesis describes experiments to study the energy levels in the nucleus ^{191}Tl populated by a heavy-ion induced reaction. The nucleus was studied previously by this group as part of a Ph.D. dissertation [1], and at another institution by Goettig *et al.* [2], providing a starting point for this work.

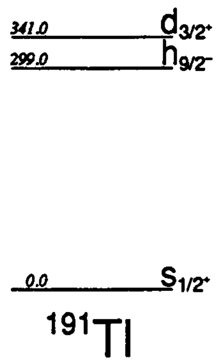

Figure 1.1: The lowest lying shell state of ^{191}Tl.

The low lying states in ^{191}Tl are well described by the shell model representative of spherical nuclei. The ground state (Fig. 1.1) is the $s_{1/2}$ orbital. The first excited state is $h_{9/2}^-$, followed by $d_{3/2}^+$. The high spin states studied in this work are built on the $h_{9/2}^-$ level which is an isomer having a lifetime of 5.22 minutes [3].

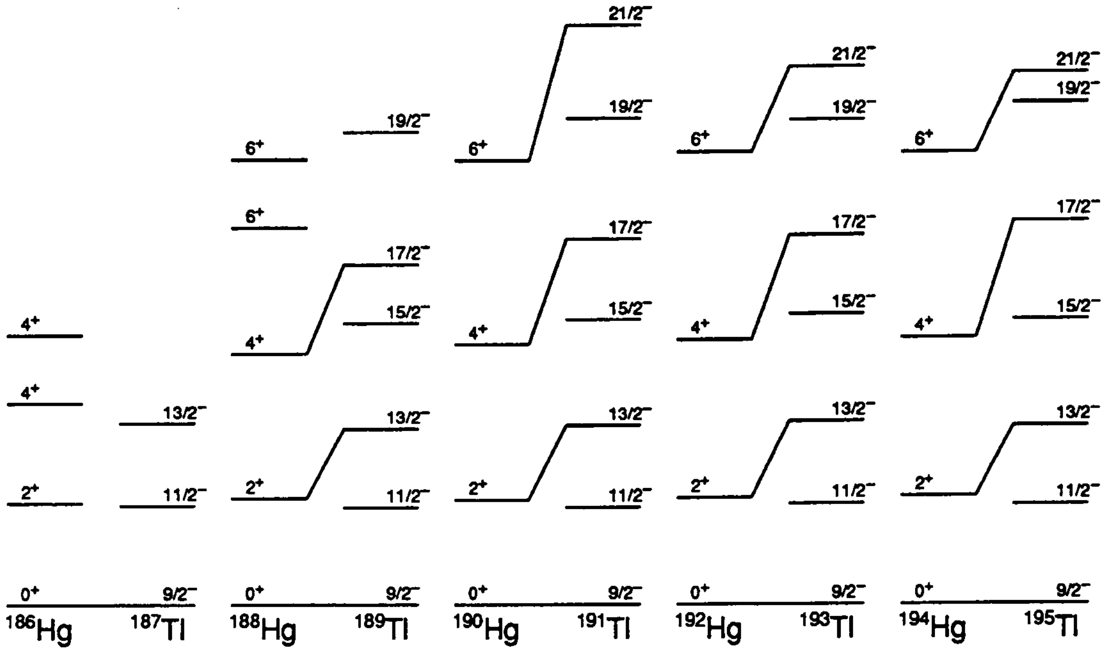

Figure 1.2: Systematics of negative parity levels in odd-A Tl nuclei compared with their respective even-A Hg cores. The sources for the different nuclei are as follows: ^{186}Hg [8]; ^{188}Hg [9]; ^{190}Hg, ^{192}Hg and ^{194}Hg [6]; ^{187}Tl [7], ^{189}Tl [10], ^{193}Tl [11], ^{195}Tl [12].

Systematics of neighboring nuclei show rotational bands built on the $\pi h_{9/2}$ [4] and $\pi i_{13/2}$ [5] configurations. This is shown in Fig. 1.2 for the negative parity $h_{9/2}$ bands of $^{187-195}$Tl, compared to their respective Hg cores. Most of the rotational bands have a slightly oblate shape, as in the ground state of the ^{190}Hg core [6] for ^{191}Tl. Until the present work, however, bands are not seen built on the positive parity $i_{13/2}$. These levels are shown compared to the $h_{9/2}{}^{-}$ level in Fig. 1.3. In addition, prolate bands have been discovered in the Hg core and in ^{187}Tl [7]. One would possibly expect to see such a prolate structure in ^{191}Tl. However, the prolate bandhead in ^{190}Hg comes much higher in energy than in ^{186}Hg, the core nucleus for ^{187}Tl. For this reason, it may be impossible to populate the prolate band in ^{191}Tl.

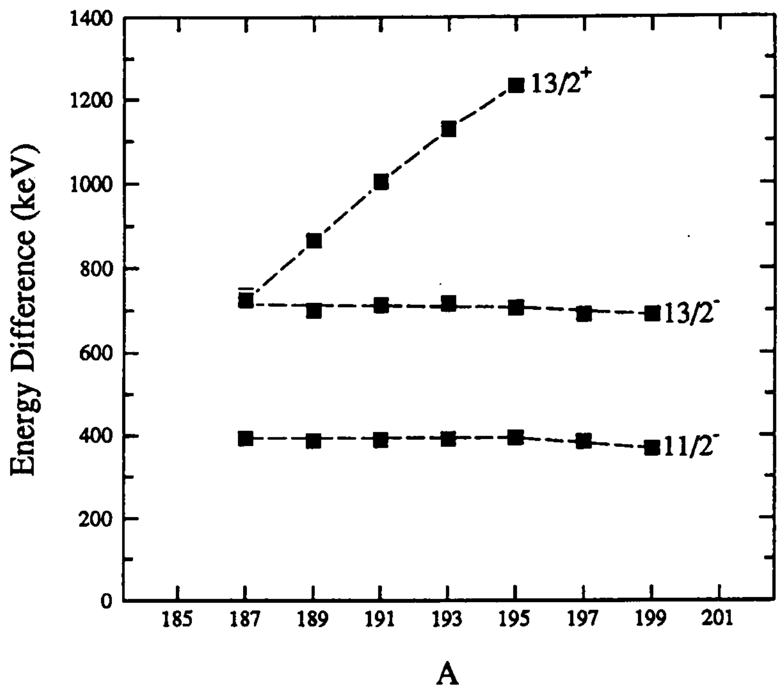

Figure 1.3: Systematics of positive and negative parity $\frac{13}{2}$ levels in odd-A Tl nuclei compared the $\frac{9}{2}^-$ level.

Besides these normal shapes, recent work by Pilotte *et al.* [13] has uncovered two superdeformed bands in ^{191}Tl. These bands are very weakly populated (about 1% of the total events), requiring a large amount of data. It is this body of data which is used herein to study the normally deformed states of the nucleus. Such large amounts of data also allow weaker normal structures to be observed.

Earlier work by Kahler and Goettig mentioned above was able to detect the beginning of a negative parity rotational band that is associated with the $\pi h_{9/2}$ orbital. Also was seen the beginnings of a positive parity structure which could be the $\pi i_{13/2}$ band. Neither of these structures reach very high in spin in the earlier work [1, 2]. The positive parity structure of the previous results, for example, does not even show rotational behavior.

A very large amount of data is available for this work, resulting from three separate experiments. Each experiment used a different arrangement of γ-ray detectors placed in large arrays, with the specific configuration of these detectors allowing better results for different types of analysis. Different target materials and beam species were also used to enhance the population of the desired nucleus. Having the advantage of large data sets and sensitive detector arrays, it is the goal of this thesis then to extend the level scheme of the normally deformed states of ^{191}Tl. In addition to extending each of these structures to higher spin and thus establishing their rotational nature, weaker non-rotational structures will also be discussed.

One way to view a nucleus like ^{191}Tl that has an unpaired valence particle is as a single particle or hole coupled to a core nucleus. Another aim of this work is to find and understand the levels in ^{191}Tl that correspond to these single-proton couplings to the spherical shapes in this region. Finally, the observed results will be compared to theory. Calculations can be performed that predict the behavior of rotational bands in the nucleus at high angular momentum when it is more greatly deformed, as well as for the nucleus at smaller values of rotational frequency when it is more nearly spherical. These calculations will be used to explain the existing and newly observed structures in ^{191}Tl.

CHAPTER 2

Experimental Setup

2.1 General Considerations

An accelerator based experiment in nuclear physics is carried out by producing an excited nucleus through the collision of a projectile nucleus with a target nucleus. If the energy of the projectile is high enough to overcome the Coulomb barrier, a union between projectile and target takes place and the energy is distributed equally to all nucleons of the fusion product (compound nucleus). Next, neutrons and perhaps protons are emitted on the way to the formation of a less excited final nucleus. For a projectile heavier than an α particle, as used in the experiments described herein, the compound nucleus and the final nucleus are formed with rather large values of angular momentum. This is desirable to study the high-spin states of the final nucleus.

There are different ways in which the compound nucleus can de-excite depending upon the excitation energy, the binding energy of the nucleons, and some other criteria like fission. The latter is a possibility in some cases, however the experimental parameters are carefully chosen to minimize this undesired pathway. The most common way for the compound nucleus to de-excite is the evaporation of neutrons, protons and α particles. In the nuclear mass region relevant for this work, neutron evaporation dominates over the evaporation of charged particles, and each neutron typically carries away about 8 MeV of excitation energy. After a few evaporation steps, the nucleus is still excited, but not highly enough to evaporate another particle. At this point the nucleus still carries a relatively high amount of angular momentum very close to the initial amount. Once this condition has been reached, the nucleus dumps its angular momentum and its remaining energy by the emission of γ rays.

The purpose of the experiments detailed in this thesis is to study the nucleus ^{191}Tl by detecting and analyzing these γ rays. This goal was accomplished using state of the art detectors grouped in large arrays. The following section explains how these detectors work and how they can be linked together to give an instrument which, along with proper analysis techniques, can be used to separate the different reaction channels and measure the γ rays. This is done as an effort to better understand the level structure of the nucleus being studied.

2.2 Collection and Recording of Events

2.2.1 Detectors

A γ ray with an energy in the range of those observed for this thesis (50 - 1500 keV) interacts with matter most probably in one of two ways; photoelectric absorption or Compton scattering. In these interaction processes the incident photon can lose all of its energy in a single interaction (absorption), or any fraction of its energy over a number of interactions (scattering). In the case of photoelectric absorption, the γ ray causes electrons to be released from their bound atomic orbitals in the detector material. Compton scattering occurs when a γ ray strikes an electron in the detector and is scattered from its original trajectory imparting kinetic energy to the recoil electron. It is the electrons directly or indirectly produced by these two interactions that are finally collected to measure the energy of the incident photon. Two different classes of detectors were used in this work: scintillation and semiconductor materials. They differ in the way the detector responds to the electrons. In the scintillation detector, the electrons produce visible light that is transformed into an (amplified) electric signal by a photomultiplier tube. Semiconductor detectors rely on the production of electron-hole pairs produced by the incident particle. These charge carriers are forced to migrate to collecting contacts by a high voltage applied across the crystal. In both cases, an energy-proportional signal is obtained.

Each of these types of detectors has its advantages and disadvantages. Semiconductor detectors made of germanium or silicon generally have higher energy resolution, however, due to a low stopping power for radiation they have a low detection efficiency. Consisting of materials with relatively high atomic numbers, scintillators, on the other hand, have larger detection efficiency. They can also be physically larger than semiconductor detectors, and hence are more likely to stop scattered photons. Two types of scintillation detectors, thallium-activated sodium iodide (NaI(Tl)) and bismuth germanate (BGO), and one type of semiconductor detector, high purity germanium (HPGe), were used in these experiments. Over the range of energies seen, the HPGe detector has a full width at half maximum (FWHM) resolution of about 1.8 keV for the 662 keV γ ray of the mono-energetic ^{137}Cs source. For comparison, NaI(Tl) has a corresponding resolution of about 46 keV, and BGO of about 100 keV [14]. For the 1173 and 1332 keV lines of the ^{60}Co source, the energy resolution of HPGe is about 2 keV whereas BGO is unable to resolve this doublet. Since most in beam γ-ray spectra have many peaks close together, it is necessary to use the HPGe detectors for spectroscopy.

In the fusion reactions used, final nuclei other than that of interest are created by successive neutron decay from the compound nucleus. Each neutron evaporation cascade is referred to as the xn channel, where x is the number of neutrons in the cascade that populated the final nucleus. At each evaporation step the nucleus is left with less energy, so it follows that a $4n$ channel leaves the resulting nucleus more highly excited than a $5n$ channel. If the nucleus is created with less excess energy, then there is not as much energy available to cause γ-ray decay, hence a $5n$ channel would have a lower number of γ rays being emitted than a $4n$ channel. The total number of γ emissions in an event is known as the multiplicity. It is measured by the number of hits in an array of detectors and is called the fold. The fold is always smaller than the multiplicity since a total counting efficiency of 100% cannot be reached.

It is possible then to separate a $5n$ channel from a $4n$ channel by analyzing the total number of γ rays which were in coincidence. Since for channel selection interest lies only in the number of γ rays and not their energies, either NaI(Tl) or BGO is the preferred choice over HPGe because they have higher counting efficiency. Many of these detectors are normally mounted in a 4π or "ball" arrangement, and are placed closely around the reaction chamber so that a large solid angle is covered. They then act as a filter to suppress Coulomb excitation on-line and aid in reaction channel selection off-line.

As mentioned before, one of the interactions of a γ ray with the detector is Compton scattering. As long as the scattered photon remains within the detector, all of its energy is included and the event is registered in the "full energy" peak for that γ ray. However, if the scattered photon escapes from the detector, there will be an incorrect energy recorded that is only a fraction of the energy of the original photon. This contributes to the "Compton distribution" below the full energy peak for that γ ray. The Compton distribution raises the background under other full energy peaks, making it difficult to detect weak γ rays. This Compton background can be significantly reduced (by a factor of 4 or 5) by placing an annular BGO counter around the HPGe crystal, and requiring anticoincidence between the two [15]. In this configuration, if a photon escapes the HPGe detector, it will be collected by the BGO annulus and the event will be vetoed. BGO is the material of choice over NaI(Tl) for this purpose due to its higher atomic number and density, resulting in a total γ-ray absorption coefficient which is about 2.2 times larger than that of NaI(Tl) [16]. This allows a smaller amount of material to accomplish the same purpose.

2.2.2 Electronics

The signals from these detectors are processed using a complicated system of electronics. Since three experiments are covered in this work, each of which was performed on a different instrument, we will only discuss the electronics in general. The main purpose of these electronics is to process and record the γ-ray energies and time of detection in order to determine whether or not two or more γ rays are in coincidence, and to either accept or reject the event based on these determinations. This requires two circuits, one for energy and one for time.

A typical energy circuit consists of a pre-amplifier, amplifier, and Analog to Digital Converter (ADC). First the signal goes through a low-noise pre-amplifier which then passes it on to the energy amplifier. This amplifier shapes the pulse, integrates the pulse over time and converts this to pulse height, which corresponds to the energy deposited in the detector. The combination of the two amplifiers maintains good energy resolution. At the end of the circuit, the signal goes on to the ADC, which converts the pulse height to a digital value that can be recorded by the data acquisition system.

The timing circuit is more complicated. Its purpose is to establish when an event happened, and essentially whether or not two γ rays were in coincidence. This determination will eventually control the data acquisition process. A second signal is taken from the pre-amplifier and fed into a timing filter amplifier, preserving the timing resolution of the pulse. The output pulse at this point still contains energy information stored in the pulse height and is about 50 ns wide. Next the signal goes into the Constant Fraction Timing Discriminator (CFTD) which has a twofold purpose. First the CFTD applies a pulse height threshold to the signal. Since pulse height still has energy information, this threshold can be used to reject low energy events such as X-rays. If the pulse crosses the threshold, a logical signal independent of the amplitude of the input pulse is created (compensation for amplitude walk [14]). This is a squared output signal which no longer carries energy information; the pulse height is set to a constant value (usually around 2 volts). The width of the pulse can be adjusted and essentially defines the "time window" for a coincidence. This is also known as the resolving time and is about twice the width of the CFTD output, *i.e.* about 100 ns. At this point the signal is sent to both a Time to Digital Converter (TDC) and a multiplicity box.

Each HPGe detector has its own set of electronics as described above. In order to determine whether events in one HPGe were in coincidence with those in another, one of the CFTD outputs from each detector is fed into a multiplicity box. This component looks for time overlap in the CFTD signals, which would indicate that two or more detectors fired within the time window and are thus in coincidence. This is known as a prompt event. Most experiments require that at least two HPGe detectors fire within this prompt window before the event is considered for being recorded. This is known as the fold of the data and is often referred to as singles, doubles or triples data, depending on how many coincidences were required. Once the coincidence criteria are met, the multiplicity box triggers the TDC to convert the timing information into a digital value that can be recorded.

In experiments where a ball is used, there are a few more steps added into the electronics. The purpose of the ball is to record the multiplicity and total energy of the γ-ray emissions for a particular event. The energy circuit for the ball detectors is similar to that for the HPGe detectors except that instead of getting an energy for each detector, all the ball detectors are summed together to get the total energy. The timing circuit likewise is similar to before. The output from the multiplicity box is fed into an event box where the ball events meet the coincidence events from the HPGe detectors. The event box puts together the multiplicity information and is a deciding point as to whether or not to accept the event. The decision is based on the total fold of the combined events. This is called a "hardware" fold cut and usually a value of four is required at this point. If these conditions are met in the event box, then it is considered a master event and the data acquisition system is opened to record the data from all the detectors.

As mentioned earlier, Compton scattering can become a problem for the small HPGe crystals so they are surrounded by a scintillator shield. This requires another set of electronics, but this time, the interest lies only in the timing information. The time signal from the HPGe detector is fed into a multiplicity box with the time signal from the shield. If there is a coincidence here, the entire event is rejected, regardless of whether the conditions described above are met or not. Events that show a coincidence between the shield and HPGe are referred to as "dirty" and are ignored. Only "clean" events are considered for processing.

2.2.3 Specific Considerations for Large Detector Arrays

A typical experimental setup will consist of many HPGe detectors placed at different angles around the reaction chamber. Since each detector has its own electronics, each has a different "gain" and although its energy information is correct, a peak of a certain energy may be in one channel in one detector and a slightly different channel in another. One could use a separate set of energy calibration coefficients for each detector, but since the detectors are usually summed, it is more convenient to gain match the detectors. This process can be done either on-line or off-line and involves calculating for each detector a set of coefficients that shifts a peak of a certain energy into the same channel in all of the detectors. In most cases the energy is not linear with channel number of the ADC. Therefore, calibration with a multiple γ-ray source like ^{152}Eu covering a range of energies is necessary to establish these coefficients from polynomial fits of the energy-channel function. Once the gains have been adjusted, it is possible to sum any combination of detectors.

Often, a thin target is used which typically consists of a metallic foil having a thickness 1 mg/cm^2 or less. With this type of target, the reaction products are expelled from the foil and emit γ rays while traveling in the direction of the beam with a non-negligible velocity, typically 1-2% the velocity of light. This "decay in flight" causes the γ-ray energies to be Doppler-shifted depending on the velocity and the direction cosine of the angle between the path of the source and the detector [17]. Consequently, each set of detectors at a given angle relative to the beam axis will experience a different Doppler-shift of the γ-ray energies recorded there. Therefore, a correction must be made to each detector depending on its angle. Although the use of a thin target introduces this complication, it is preferred over a thick target for our purposes. A target could be used that is thick enough to stop all reaction products and thus eliminate the emission of γ rays in flight. In this case, however, as the reaction products decelerate in the target material, a distribution of velocities is obtained causing the energy peaks to be Doppler broadened.

Usually these two adjustments are made off-line by reading, correcting and rewriting the data event by event. This is a time consuming process and normally would not be done on-line because it would severely slow down the data acquisition. One big advance in the area of data processing is the advent of parallel computers. With this technology it is possible to manipulate the data on-line without appreciably slowing the recording of data. Such a computer system was used in Experiment 2, which will be discussed later.

2.3 Experiments

Each of the following experiments was performed primarily to search for superdeformation in ^{191}Tl, resulting in the discovery of two superdeformed bands [13]. The purpose of this thesis is a detailed analysis of the data from these experiments to study the normally deformed states of ^{191}Tl.

2.3.1 Coincidence Experiment on the Spin Spectrometer

The first experiment was performed at the Holifield Heavy Ion Research Facility (HHIRF) located at the Oak Ridge National Laboratory (ORNL). A beam of ^{36}S with an energy of 165 MeV was focused onto a ^{159}Tb target to produce ^{191}Tl through the $4n$ channel. The target consisted of a stack of two foils with a thickness of 0.5 mg/cm^2 each to obtain fully Doppler-shifted peaks with only one component. Data were collected using the Spin Spectrometer in conjunction with 19 Compton suppressed HPGe detectors (CSGs). The Spin Spectrometer is a NaI(Tl) array that approximates a hollow sphere with an inner radius of 17.8 cm [18] and in this experimental application consisted of 52 detector elements. Each valid event was defined by the requirement that a minimum of two CSGs fire in prompt coincidence with a minimum of six NaI(Tl) elements. Approximately 120 hours of beam time were used to collect about 200 million double and higher fold CSG events. This data set was essentially used to confirm the previously known level scheme of ^{191}Tl [1, 2] and begin to extend the scheme.

2.3.2 Coincidence Experiment on the Compact Ball

A second experiment on ^{191}Tl was performed at HHIRF, using a different reaction, ^{169}Tm(^{26}Mg,4n), at a beam energy of 128 MeV. Again a stacked target of two 0.5 mg/cm^2 foils was used. In this case, data were taken with the Compact Ball [19] which consists of 20 CSGs located closer to the target than the CSGs in the Spin Spectrometer. Mainly due to this geometry, higher counting efficiency was obtained for the CSGs making it possible to collect 500 million triple coincidence events in approximately 120 hours.

The larger number of events helps to add more sensitivity for weak transitions, however, the absence of an inner ball makes it more difficult to separate the contributions from other reaction products in the γ-ray spectrum. As mentioned above, the gain matching including a Doppler correction was done on-line. Care was taken to check the gain matching throughout the run to compensate for gain drifts in individual detectors. The large number of events in this data set was used to establish the coincidence relationships that led to the construction of the level scheme, and to evaluate all the γ-ray intensities, I_γ.

2.3.3 Coincidence Experiment on the Detector Array at Argonne

In the third experiment, the same reaction as in Experiment 1, ^{159}Tb(^{36}S,4n) was used. The beam at an energy of 165 MeV was provided by the Argonne Tandem Linac Accelerator System (ATLAS), located at Argonne National Laboratory (ANL). A thin target made of two 0.5 mg/cm^2 foils was used. The detector array consisted of 12 CSGs and an inner BGO ball of 50 elements. Four elements of the inner ball were required to fire in prompt coincidence with a minimum of two CSGs. Approximately 120 million events were recorded. In the γ-ray detector facility at Argonne, the CSGs are located at 34.5°, 90°, and 146.5°with respect to the beam axis. These data were used to measure the γ-ray directional correlations of the newly observed transitions in ^{191}Tl.

2.4 Analysis

The purpose of the data analysis is to obtain a detailed level scheme. A level scheme contains information on the excitation energy, angular momentum, and parity of each level and it is the essential step towards an understanding of the nuclear structures involved. Three pieces of information are used and combined in the process of building a level scheme. First it is necessary to investigate the coincidence relationships between γ rays. Secondly, the intensity of each transition is analyzed. And thirdly, the multipolarity of each transition is derived from the angular distribution information. In the first two steps the level scheme is constructed. The last step is necessary to further test and finally establish the scheme. Powerful software packages have been developed and introduced into the process of data analysis and they enable one to evaluate the data very precisely and efficiently. This section deals with the techniques of the building of the level scheme for ^{191}Tl. How the results are used to piece things together will be discussed in detail throughout Chapter 3.

2.4.1 Building and Handling of the γ-γ Coincidence Matrix

In order to establish the coincidence relationships, a two dimensional E_γ-E_γ histogram is constructed, referred to as a γ-γ coincidence matrix. This matrix is built by incrementing the (E_1,E_2) cell for each coincidence of two γ rays with energies E_1 and E_2. An event containing three γ rays (E_1, E_2, E_3) in coincidence is resolved into three pairs, *i.e.* (E_1,E_2), (E_1,E_3) and (E_2,E_3). Only (E_1,E_2) coincidence events with specific time relationships are considered by gating on the prompt peak of the time spectrum and by subtracting the part of the time spectrum which corresponds to random coincidences. In the matrix, the intensity I(E_1,E_2) of each cell corresponds to the number of counts recorded for that specific (E_1,E_2) combination. To ease the further analysis of the coincidences, the matrix is usually symmetrized by transposing the original matrix and adding the original and transposed matrices together.

Another function of the matrix is to have a selected set of data with the desired reaction product enhanced. As mentioned earlier, the "ball" detectors can be used as a multiplicity filter. By setting criteria in the sorting routine that builds the matrix, it is possible to select any range of multiplicities and thus virtually eliminate some reaction channels from the matrix.

Once this matrix is obtained, it is "sliced" on one axis and the content of the slice is projected onto the other axis. Since the matrix is symmetric, it makes no difference which axis is chosen. Each of these projections is known as a gate and each gate is related to a specific γ-ray energy. Since the axes represent energy, each gate is actually a spectrum of the γ-ray energies in coincidence with the γ ray that corresponds to the position of the gate.

As described in Section 2.2.1 there are two types of γ radiation expected in a matrix; photo peaks appearing as discrete lines and a large continuous background mainly due to Compton scattering. This background must be subtracted to obtain a clean coincidence spectrum. For a coincidence matrix, the background is usually independent of the energy. Therefore a "universal" smooth background can be drawn from the spectrum and used for all channels. This has been done for the analysis of the coincidence data described here. In the final matrix, background was subtracted and essentially only discrete lines were present.

By comparing several gates with each other and examining the energies contained in each gate, it is possible to build coincidence/anticoincidence relationships between the γ rays in the data. A step by step example of how this has been done is given in Section 3.2.

2.4.2 γ-Ray Energies and Intensities

To determine the energies and intensities of the γ rays considered, it is necessary to have energy and efficiency calibrations for the detector system. During the experiment, calibration runs with the radioactive sources ^{152}Eu and ^{133}Ba were performed. An energy calibration is obtained from these source data by measuring the positions of known photo peaks. The areas under these photo peaks correspond to intensity and are used to determine the relative detection efficiency of the CSGs as a function of γ-ray energy. The measured efficiency data is shown in Fig. 2.1

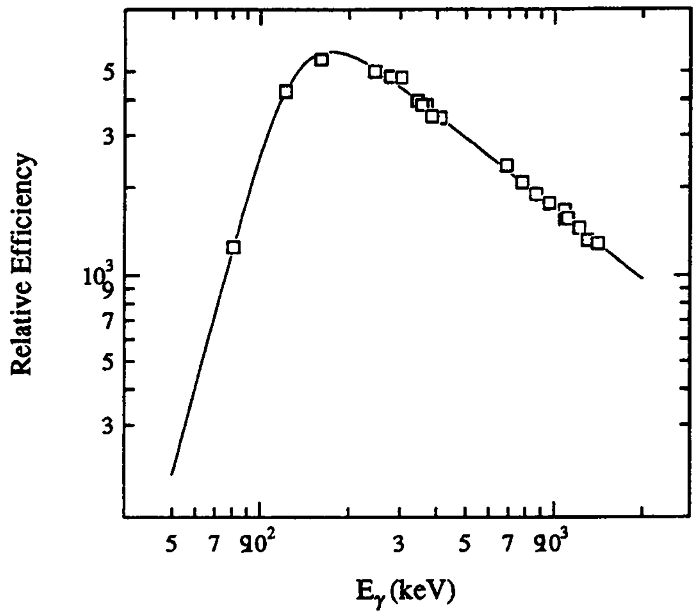

Figure 2.1: Measured relative efficiency (^{152}Eu, ^{133}Ba) and fitted curve for the HPGe detectors used in the Compact Ball run (Experiment 2). Error bars of the data points are within the symbol size.

along with a curve fitted to these points. The data points are obtained from building the ratios between the measured peak areas and accepted relative intensities for these peaks [20]. The ^{133}Ba source gives the low energy part of the curve and ^{152}Eu is used for the higher energy portion. The program EFFIT by D. Radford is used to fit these points to an empirical expression given in reference [21]. The resulting efficiency curve can be used to create a table of efficiency factors for each energy, or it can be used to make a spectrum which can be applied to the matrix as a whole or used on individual gates. The latter method was used in this work. Each gate or projection was divided by the efficiency spectrum before it was used to get the areas under the peaks representing their intensities.

The peak areas for the in-beam spectra which follow were analyzed with the program GF2 by D. C. Radford [22]. In GF2, least squares fitting is used to approximate the line shape of a photoelectric peak with a Gaussian plus a skewed Gaussian (for the often apparent low energy tail). A polynomial fit is used for the background. From the fit, a peak centroid and peak area are determined.

The γ-ray intensities are given as relative intensities, *i.e.* normalized to the intensity of the strongest peak. To do this one starts with the "total projection" of the γ-γ matrix containing all the events and fits all the peaks. In ^{191}Tl, the 388 keV transition is known to be the most intense one, hence this transition is used for normalization. Taking the total projection instead of evaluating peak intensities in a gated spectrum has the advantage that the effect from side-feeding transitions that might exist and bypass the gating transition is eliminated. However, the total projection is only useful for the evaluation of the transitions which are strong and "clean," that is, those which are not doublets, contaminants, or otherwise too close in energy to another transition in the nucleus under study or in some other reaction product.

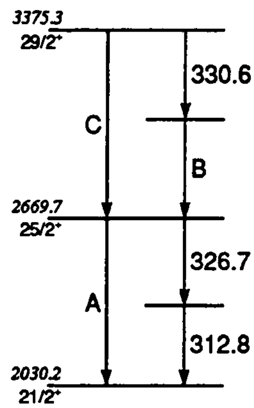

Figure 2.2: Example of using ratios to determine intensity by comparison to known transitions.

For those transitions which are not clean, the intensity must be found by some other method. This can be accomplished by using a gate and getting area ratios between a transition of known intensity and the one desired. An example is given in Fig. 2.2. In this case, the intensity of C is known and we are trying to determine the intensity for B. First, one would make a gate on the transition A, and from this gate find the areas of peaks B and C. The intensity of peak B then would be:

$$I_\gamma(B) = I_\gamma(C)\frac{Area(B)}{Area(C)}. \tag{2.1}$$

This method can also be used to gate on a transition above the level and look at the transitions decaying from that level.

The intensities considered so far are due only to the γ-ray emission and hence are denoted I_γ. In order to be able to use the intensity information as a check of the level intensity balances, one must take into account that only part of the decay intensity is carried by γ radiation. Another part, however, proceeds by internal conversion, *i.e.* by the emission of orbital electrons. The relative amount of intensity used in the process of internal conversion depends on both the energy and multipolarity of the nuclear transition. For example, an $M1$ transition is more converted than an $E1$ transition or an $E2$ transition with the same energy. This behavior is usually described by the conversion coefficient (α) which is the ratio of the electron emission rate to the γ-emission rate. The decay intensity I of a particular nuclear transition is then given by:

$$I = I_\gamma(1 + \alpha_T), \tag{2.2}$$

where α_T is the total probability for an emission from one of the K-, L-, or M- atomic subshells. The values of α_T are the subject of tables [23]. These tables give values of α_T at certain transition energies. For this work, these values were plotted as a function of energy and fit with a polynomial regression to obtain the interpolated values of α_T for the specific transition energies in ^{191}Tl. These values were used for determining the decay intensities.

2.4.3 Directional Correlation of γ rays

In (HI,xn) reactions, the nuclei are populated in states with "alignment" *i.e.* the spins are oriented in a plane perpendicular to beam axis. This alignment is not greatly affected by subsequent emissions of neutrons and γ rays. The γ rays emitted from these spin states have a certain angular distribution, *i.e.* their intensity depends on the angle between the spin direction and the direction of emission. Very characteristic but different radiation patterns are obtained for different γ-ray multipolarities (such as $M1$, $M2$, $E1$, $E2$ radiation) [24].

In principle, these patterns could be measured with one detector by changing the detector angle with respect to the beam axis. In multi-detector arrays, however, the CSGs are located at fixed angles. Thus, directional correlations between γ-ray are measured which – like the angular distributions – enable one to determine the level spins through the multipolarities. For those transitions that are not purely of one type of multipolarity, it may be possible to determine mixing ratios. Directional Correlations of γ rays from Oriented nuclear states (DCO) as discussed in reference [25] have been measured with detector arrays to a great extent and were successfully used to derive the multipolarities of γ rays, see *e.g.* reference [26].

The intensities of a peak detected at different angles with respect to the beam axis need to be compared in order to measure the γ-ray anisotropy of a particular transition. The comparison is done by the corresponding intensity ratio referred to as a DCO ratio. For this comparison, angle positions close to 90° and close to 0°

and 180° should be available to obtain a large effect in the DCO ratios. Then the DCO ratios are grouped around a certain reference value for stretched quadrupoles ($I \rightarrow I-2$) and a distinctively different reference value for stretched dipoles ($I \rightarrow I-1$); mixtures fall somewhere in between. The actual reference values of the DCO ratios change, of course, from instrument to instrument.

The DCO ratios were extracted from the data from Experiment 3. At Argonne, the setup for the HPGe detectors of the array is as follows. Four pairs of detectors are placed at ±34.5° and ± 145.5° with respect to the beam axis (forward and backward angles), and two pairs are placed at 90°, making for a total of 12 detectors. The DCO ratios were extracted according to the following definition:

$$R = \frac{I(\gamma_1(145.5^\circ), \gamma_2(34.5^\circ))}{I(\gamma_1(90^\circ), \gamma_2(34.5^\circ))} \approx \frac{I(\gamma_1(145.5^\circ))}{I(\gamma_1(90^\circ))}, \tag{2.3}$$

where I denotes the intensity. The observed transition γ_1 is detected at ±145.5° or± 90°. The gating transition γ_2 is always detected at the forward angles of ±34.5°.

The procedure using this definition has the advantage that consistently the same reference values for stretched quadrupoles and dipoles are obtained for γ_1 regardless of whether the gating transition γ_2 is a quadrupole or a dipole [27]. In other words, R depends only on the multipolarity of the γ ray observed (γ_1) and is independent of the γ ray on which a gate is applied. For the setup at Argonne, the reference values are 0.71 for stretched dipole transitions and 1.39 for stretched quadrupole transitions [27].

For the DCO analysis, a separate set of two angle sorted E_γ-E_γ matrices was prepared: one for the combination of the coincidence of transitions in the 90° and forward angle detectors, and the other for the forward and backward angles. In this scenario the forward angle was used as the gating angle, which helped to avoid cases with large neutron background in the gated spectra at the side angles, since neutrons are primarily observed in the forward angle.

By gating on different structures it is often possible to obtain separate DCO ratios for peaks which appear as doublets. However, in cases where gating is of no help, it is still possible to get a reasonable estimate of the nature of the transition. It was noticed during the analysis that if one peak in a doublet was of dipole and the other of quadrupole nature, the ratio was much higher than would be expected for a dipole transition. On the other hand, if both members of the doublet were of the same nature, the resulting ratio would be very close to what was expected. This approximation, however, assumes that the transitions in question are pure in nature and not dipole/quadrupole mixtures.

CHAPTER 3

Experimental Results

3.1 Construction of the Level Scheme

From a detailed analysis of the "total" and angle sorted γ-γ coincidence matrices described in the previous chapter a new level scheme for ^{191}Tl has been constructed. This level scheme is presented in Fig. 3.1. A number of γ rays coincident with each other form a sequence in the scheme. The ordering within a sequence is based on the intensities. Principally, the intensity of the transition decreases when moving upwards in the scheme because of observed and unobserved (very weak) side feeding. Special care is taken that the transition intensities between consecutive levels are in balance. If in the process of constructing the scheme, more intensity was seen going into a level than is coming out, then it was most likely that a transition from that level had escaped our attention – such cases are ruled out in the presented scheme. The multipolarities obtained from DCO ratios are often supporting evidence. This is in particular the case when a pair of transitions with dipole character is bypassed by a transition of quadrupole character. Three main structures are present in the level scheme and have been numbered from 1 to 3 to make the following discussion (Sections 3.2 - 3.4) more transparent.

Previous studies of level structures in ^{191}Tl have served as a starting point for the new level scheme. In particular the previously known level assignments are, together with our DCO ratios, the basis for spin and parity assignments to new levels. Our study begins at the $\frac{9}{2}^-$ level at an excitation energy of about 300 keV which is an isomer having a lifetime of 5.22 minutes [3]. Because the lifetime

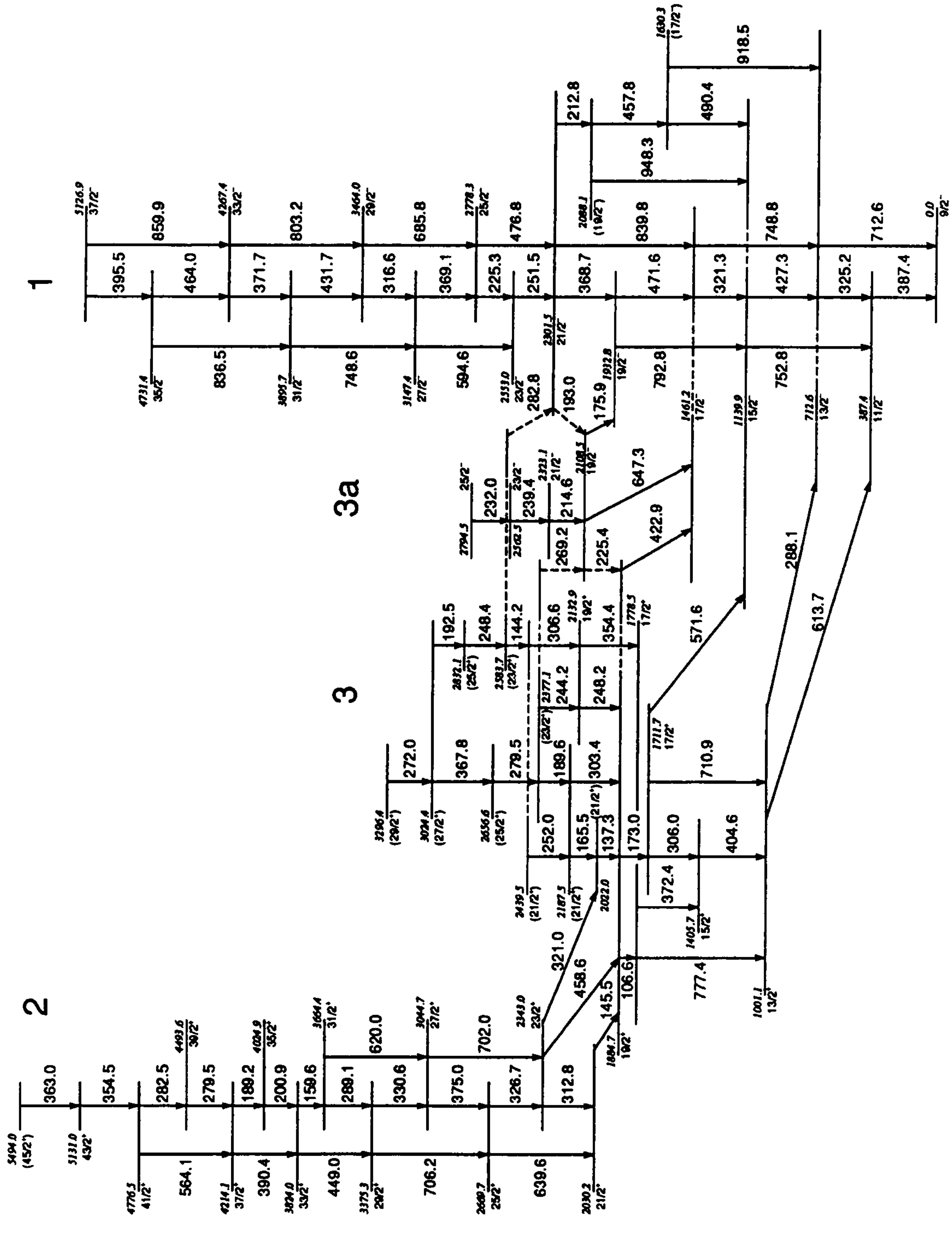

Figure 3.1: Proposed level scheme for ^{191}Tl. Spins and parities given in parentheses are tentative. Level energies are given in reference to the isomeric $\frac{9}{2}^-$ state (see text).

is long compared to our coincidence window of about 100 ns (see Section 2.2.2), one would not expect to see any of the structure below this level in these data. Therefore, the first level shown in the scheme in Fig. 3.1 is not the actual ground state for this nucleus. For purposes of convenience, this level was assigned an energy of zero and all the other energy levels reported are given relative to this reference energy. Previous work on higher spin states by Kahler [1] and by Goettig *et al.* [2] established states built on the $\frac{9}{2}^-$ isomer up to spins of $\frac{21}{2}^-$ and $\frac{17}{2}^+$ respectively.

The Table 3.1 summarizes the pertinent data that were used in concert with the coincidence gates to propose the level scheme shown in Fig. 3.1. The first column gives the energy of each transition in keV to within 0.2 keV. These are ordered numerically so that doublets can easily be identified. The second column contains the γ-ray intensities, I_γ for each transition. There are two problem cases, the 200.9 and 248 keV transitions. In both cases it was not possible to separate the members of the multiplet present in the data. Therefore the value reported is for the multiplet, not the individual γ ray, and should be viewed as an upper limit. Column three reports the DCO ratios which were measured as detailed in Section 2.4.3. DCO ratios are reported for all but four transitions. The reason for missing values is that in the appropriate DCO gates these peaks were too weak to get a reliable value. In the case of the 835.9 keV transition there was the additional complication of contamination; although it was not possible to get a value, it was evident from inspection that this transition was of a quadrupole nature. These ratios were used in determining the assignment of each transition as either dipole, quadrupole, or a mixture thereof. This assignment is shown in the following column. Since not all of the intensity from a given level is represented by I_γ, one must include the intensity which goes toward the internal conversion. This calculation was given

Table 3.1: Experimental results.

Transition Energy (keV)	Gamma Ray Intensity	DCO Ratio	Assign.	Decay Intensity	Band	Initial Level E_i (keV)
106.9	5.08 ± 0.40	0.6369 ± 0.0890	D	35.83 ± 2.83	3	1884.7
128.7	15.15 ± 1.49	0.7073 ± 0.0874	D	67.83 ± 6.67	U	—
137.3	6.02 ± 0.66	0.6369 ± 0.0890	D	23.25 ± 2.53	3	2022.0
144.2	2.44 ± 0.27	0.9241 ± 0.0730	D	8.46 ± 0.92	3	2583.7
145.5	14.80 ± 1.61	0.7676 ± 0.0491	D	50.33 ± 5.47	2-3	2030.2
159.6	8.97 ± 1.22	0.7818 ± 0.0723	D	25.17 ± 3.42	2	3824.0
165.5	4.78 ± 0.52	—	D	12.49 ± 1.36	3	2187.5
173.0	21.54 ± 1.70	0.8653 ± 0.0361	D	51.81 ± 4.09	3	1884.7
175.9	2.09 ± 0.91	—	D	4.86 ± 2.12	2-1	2108.5
189.2	11.40 ± 1.38	0.6224 ± 0.0453	D	23.42 ± 2.84	2	4214.1
189.6	3.40 ± 0.37	0.6224 ± 0.0453	D	6.96 ± 0.76	3	2377.1
192.5	3.08 ± 1.01	0.6835 ± 0.0750	D	6.13 ± 2.00	3	3024.4
193.0	1.57 ± 0.34	0.6835 ± 0.0750	D	3.13 ± 0.68	1-3	2301.5
200.9	16.05 ± 1.56	0.8957 ± 0.0514	D	29.94 ± 2.91	2	4024.9
200.9					U	—
209.0	8.83 ± 1.29	1.1752 ± 0.1045	Q	10.05 ± 1.47	U	—
212.8	8.69 ± 2.04	0.8139 ± 0.0843	D	14.87 ± 3.49	1	2301.5
214.6	8.62 ± 1.90	0.8037 ± 0.1511	D	14.57 ± 3.21	3	2323.1
217.2	6.39 ± 1.27	—	D	10.63 ± 2.11	U	—
225.3	14.45 ± 1.48	0.7043 ± 0.0317	D	22.87 ± 2.34	1	2778.3
225.4	7.31 ± 0.80	1.0446 ± 0.1109	D	11.57 ± 1.27	3	2108.5
232.0	4.80 ± 1.12	1.0353 ± 0.0650	D	7.31 ± 1.71	3	2794.5
233.7	3.61 ± 1.12	0.9464 ± 0.1046	D	5.46 ± 1.69	U	—
239.4	7.51 ± 1.48	0.8360 ± 0.0455	D	11.00 ± 2.17	3	2562.5
244.2	4.59 ± 1.05	0.6957 ± 0.0707	D	6.57 ± 1.50	3	2377.1
248.2	3.71 ± 0.40	0.4263 ± 0.0730	D	5.21 ± 0.57	3	2132.9
248.4					3	2132.9
251.5	25.50 ± 1.89	0.8041 ± 0.0269	D	35.31 ± 2.62	1	2553.0
252.0	0.98 ± 0.11	0.7663 ± 0.1011	D	1.35 ± 0.15	3	2439.5
269.2	4.93 ± 1.33	1.2311 ± 0.1302	Q	4.71 ± 1.27	3	2377.1
272.0	9.28 ± 3.04	0.8279 ± 0.0965	D	11.85 ± 3.88	3	3296.4
275.0	8.06 ± 1.28	0.6583 ± 0.0849	D	10.19 ± 1.62	U	—
279.5	7.48 ± 2.99	0.8737 ± 0.0746	D	9.31 ± 3.72	3	2656.6
279.5	4.18 ± 1.47	0.8238 ± 0.1063	D	5.20 ± 1.83	2	4493.6
282.5	3.99 ± 1.41	0.7719 ± 0.0835	D	4.91 ± 1.74	2	4776.5
282.8	1.47 ± 0.21	0.9326 ± 0.1189	D	1.81 ± 0.26	3-1	2583.7
288.1	5.93 ± 0.31	1.3210 ± 0.1510	D	7.18 ± 0.38	3	1001.1
289.1	14.71 ± 4.06	0.8024 ± 0.0448	D	17.77 ± 4.90	2	3664.4
295.8	7.02 ± 1.34	0.8646 ± 0.0628	D	8.32 ± 1.59	U	—

Table 3.1: (continued)

Transition Energy (keV)	Gamma Ray Intensity	DCO Ratio	Assign.	Decay Intensity	Band	Initial Level E_i (keV)
303.4	5.21 ± 0.57	0.4215 ± 0.0376	D	6.05 ± 0.66	3	2187.5
306.0	31.50 ± 4.08	0.9191 ± 0.0207	D	36.33 ± 4.71	3	1711.7
306.6	3.50 ± 1.75	0.9191 ± 0.0207	D	4.03 ± 2.02	3	2439.5
312.8	23.56 ± 1.86	0.5263 ± 0.0239	D	26.73 ± 2.11	2	2343.0
316.6	10.56 ± 1.37	0.5286 ± 0.0480	D	11.88 ± 1.54	1	3463.6
321.1	4.75 ± 0.52	0.8372 ± 0.0812	D	5.28 ± 0.57	2-3	2343.0
321.3	7.93 ± 1.44	0.8655 ± 0.0565	D	8.83 ± 1.60	1	1461.2
325.2	17.90 ± 3.84	1.0596 ± 0.0602	D	19.76 ± 4.24	1	712.6
326.7	14.90 ± 1.42	0.5729 ± 0.0220	D	16.40 ± 1.56	2	2669.7
330.6	13.76 ± 1.54	0.6817 ± 0.0370	D	15.02 ± 1.68	2	3375.3
336.0	8.76 ± 1.49	0.7735 ± 0.0537	D	9.46 ± 1.61	U	—
348.7	2.79 ± 1.12	0.9759 ± 0.1391	D	2.94 ± 1.18	U	—
354.4	10.70 ± 1.37	0.6377 ± 0.0612	D	11.20 ± 1.43	U	—
354.4	7.12 ± 2.85	0.6377 ± 0.0612	D	7.45 ± 2.98	3	2132.9
354.5	3.58 ± 1.43	0.6377 ± 0.0612	D	3.75 ± 1.50	2	5131.0
363.0	2.08 ± 0.81	—	D	2.15 ± 0.84	2	5494.0
367.8	4.93 ± 1.61	1.0949 ± 0.1161	D	5.06 ± 1.65	3	3024.4
368.7	5.05 ± 0.66	0.6657 ± 0.0293	D	5.17 ± 0.68	1	2301.5
369.1	18.54 ± 2.11	0.6657 ± 0.0293	D	18.98 ± 2.16	1	3147.0
371.7	4.90 ± 0.65	0.6274 ± 0.0835	D	5.00 ± 0.66	1	4267.0
372.4	6.06 ± 2.33	0.6637 ± 0.0445	D	6.18 ± 2.37	3	1778.5
375.0	17.65 ± 1.91	0.5855 ± 0.0316	D	17.93 ± 1.94	2	3044.7
387.4	100.00 ± 4.91	0.8884 ± 0.0172	D	100.00 ± 4.91	1	387.4
390.4	13.07 ± 1.93	1.0240 ± 0.1389	D	13.02 ± 1.92	2	4214.1
395.5	5.14 ± 1.19	0.4352 ± 0.0442	D	5.09 ± 1.18	1	5126.5
404.6	44.61 ± 2.60	0.8515 ± 0.0238	D	43.77 ± 2.55	3	1405.7
422.9	5.77 ± 4.10	0.8027 ± 0.0789	D	5.56 ± 3.95	3-1	1884.7
427.3	15.91 ± 2.16	0.8303 ± 0.0608	D	15.28 ± 2.07	1	1139.9
431.7	6.88 ± 2.93	0.5754 ± 0.0601	D	6.58 ± 2.80	1	3895.3
449.0	5.07 ± 1.40	1.5616 ± 0.2919	Q	4.34 ± 1.20	2	3824.0
457.8	11.19 ± 1.58	0.6004 ± 0.0676	D	10.50 ± 1.48	1	2088.1
458.6	3.02 ± 0.33	1.1679 ± 0.2020	Q	2.58 ± 0.28	2-3	2343.0
464.0	5.84 ± 1.40	0.9693 ± 0.1476	D	5.45 ± 1.31	1	4731.0
471.6	7.51 ± 1.48	0.7168 ± 0.1243	D	6.98 ± 1.38	1	1932.8
476.8	11.33 ± 1.65	1.2079 ± 0.0931	Q	9.64 ± 1.40	1	2778.3
490.4	8.29 ± 1.29	0.8743 ± 0.0768	D	7.63 ± 1.18	1	1630.3
564.1	6.32 ± 2.23	1.1146 ± 0.1326	Q	5.33 ± 1.88	2	4776.5
571.6	10.98 ± 2.05	0.7766 ± 0.0840	D	9.76 ± 1.82	3-1	1711.7
594.6	12.47 ± 1.28	1.2616 ± 0.1996	Q	10.50 ± 1.08	1	3147.0

Table 3.1: (continued)

Transition Energy (keV)	Gamma Ray Intensity	DCO Ratio	Assign.	Decay Intensity	Band	Initial Level E_i (keV)
613.7	91.66 ± 4.82	0.9513 ± 0.0204	D	80.56 ± 4.24	3-1	1001.1
620.0	12.72 ± 6.69	1.4386 ± 0.0845	Q	10.69 ± 5.62	2	3664.4
639.6	17.37 ± 1.77	1.3739 ± 0.1109	Q	14.59 ± 1.49	2	2669.7
647.3	16.19 ± 2.29	1.0044 ± 0.1196	D	14.12 ± 2.00	3	2108.5
685.8	15.98 ± 1.82	1.7725 ± 0.3083	Q	13.40 ± 1.53	1	3463.6
702.0	23.56 ± 2.24	1.3772 ± 0.1134	Q	19.74 ± 1.88	2	3044.7
706.2	32.87 ± 2.56	1.3735 ± 0.0860	Q	27.53 ± 2.14	2	3375.3
710.9	44.61 ± 5.77	1.1190 ± 0.0492	Q	37.36 ± 4.83	3	1711.7
712.6	57.58 ± 12.35	1.2419 ± 0.0580	Q	48.22 ± 10.34	1	712.6
748.6	22.82 ± 2.96	1.2729 ± 0.0797	Q	19.09 ± 2.48	1	3895.3
748.8	57.82 ± 10.49	1.2729 ± 0.0797	Q	48.38 ± 8.78	1	1461.2
752.8	31.83 ± 6.83	1.3765 ± 0.0771	Q	26.63 ± 5.71	1	1139.9
777.4	9.45 ± 3.63	1.4618 ± 0.1523	Q	7.90 ± 3.04	3	1778.5
792.8	15.64 ± 2.83	2.0800 ± 0.2635	Q	13.07 ± 2.37	1	1932.8
803.2	14.26 ± 6.65	1.0000 ± 0.1370	Q	11.92 ± 5.56	1	4267.0
836.5	25.37 ± 3.38	—	Q	21.18 ± 2.82	1	4731.0
839.8	45.30 ± 5.90	0.9102 ± 0.0646	Q	37.83 ± 4.93	1	2301.5
859.9	12.16 ± 1.72	2.0690 ± 0.4675	Q	10.15 ± 1.44	1	5126.5
918.5	11.61 ± 1.45	0.7774 ± 0.1029	D	9.82 ± 1.23	1	1630.3
948.3	5.30 ± 1.82	0.6059 ± 0.1126	D	4.47 ± 1.54	1	2088.1

in entirety in Section 2.4.2 and depends on both the energy and multipolarity of the transition. The resulting intensity is given in the fifth column and was used to determine intensity balances. The last two columns are read directly from the level scheme and are included to identify the transitions with those in the level scheme more easily. As already mentioned, "Band" is simply a number given to the different structures in the level scheme and places a given transition in one of the three observed. The value E_i (in keV) denotes the energy of the initial level from which the transition originates and is given in the last column. The table contains an entry for each transition in the level scheme plus a few others that appear to be related to this nucleus, but which we were not able to place. These are marked with the symbol "U" for unplaced.

The DCO ratio is very useful to determine the multipolarity of a transition. The reference values for the data set used are 0.71 for a stretched dipole ($I \rightarrow I-1$) transition and 1.39 for a stretched quadruple ($I \rightarrow I-2$), see Section 2.4.3. Dipole transitions of I to I type are expected to have a ratio greater than 1.39. Many transitions are probably not pure, but are dipole-quadrupole mixtures. These are expected to lie between 0.71 and 1.39 for a positive value of the $M1/E2$ mixing ratio or below 0.71 for a negative mixing ratio. The data from the DCO analysis and the reference values are graphically represented in Fig. 3.2. In this figure, the expected separation between dipole and quadrupole transitions is quite obvious, *i.e.* groupings of data points around the "reference lines" (at 0.71 and 1.39). And, there is a strong group of mixed transitions between these bounds.

A brief glimpse at the graph might cause one to think that a relationship exists between DCO ratio and energy, perhaps even that one might be a function of the other, but this is not entirely so. There is a noticeable pattern of lower energy transitions having ratios closer to the dipole line and those of higher energies tending toward the quadrupole line. This can be explained more so from looking at the level scheme. Notice that most of the higher energy transitions bypass two transitions which would force them to be $I \rightarrow I-2$ transitions and thus be of a quadrupole nature. The transitions that are bypassed by these bypasses are then forced to be either dipoles or of some mixed nature. This helps to explain why, for the most part, higher energies have DCO ratios that lie along the quadrupole line.

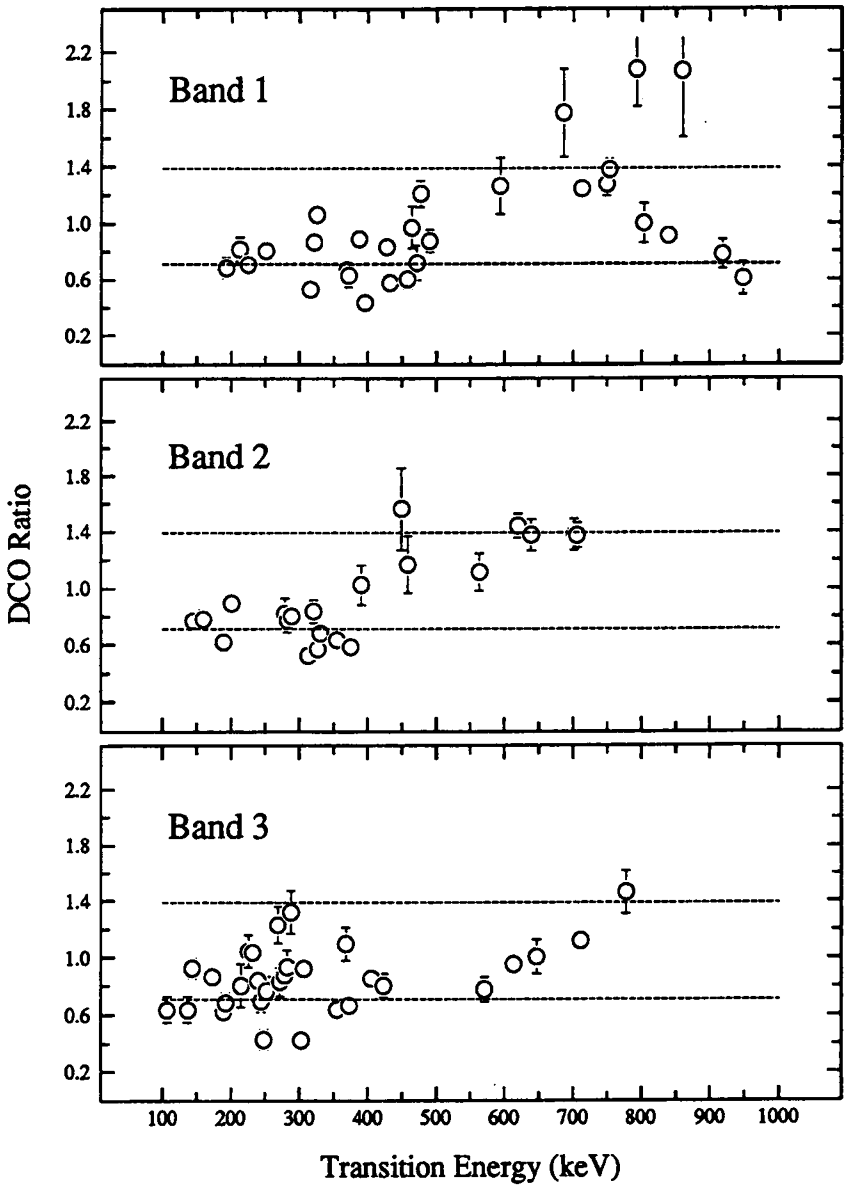

Figure 3.2: DCO ratios vs. energy. The dotted lines at 0.71 and 1.39 are reference lines for the values of DCO ratio that indicate dipole and quadrupole nature respectively.

3.2 The $h_{9/2}^-$ Band (Band 1)

Let us begin our discussion of the level scheme with Band 1. This band has a rotational-like E_γ vs. I behavior for the $E2$ transitions. It contains also relatively strong $M1$ transitions that are "bypassed" by $E2$ crossover transitions which increase in energy with spin. Feeding the $\frac{19}{2}^-$ level (1932.8 keV), there is apparently an $E2$ transition of 620.2 keV missing, after which, the $E2$ energy values take a sharp drop and then continue to increase with spin as before. This region of the band appears to be influenced by a backbend, which would be caused by the alignment of a pair of $i_{13/2}$ neutrons in this case. The backbend behavior and reasons for it will be discussed more fully in Section 4.4. It is important to mention at this time, however, that around a sharp backbend it is normal for other transitions to be seen which do not follow the same orderly progression as the rotational band. Examples of this behavior are the 212.8, 457.8, 918.5 and 948.3 keV transitions. These are associated with the non-yrast members of the two crossing bands that cause the backbend.

As indicated earlier, this band was constructed using coincidence gates. A representative example of such a gate is given in Fig. 3.3 (gate on the 427.3 keV transition). In parts of the spectrum where a doublet appears or one peak is very close in energy to a neighboring peak, both energies are then given in a single marker. The band assignment for each peak follows the energy and they are separated by a colon. Some peaks are marked that remain unplaced and are designated "U". This format will be used in all gated spectra shown in this work. From the spectrum in Fig. 3.3, one can see some transitions in Band 1 plus a few others that feed from other structures. Notice that the 752.8 keV γ ray is not present in this gate, but the

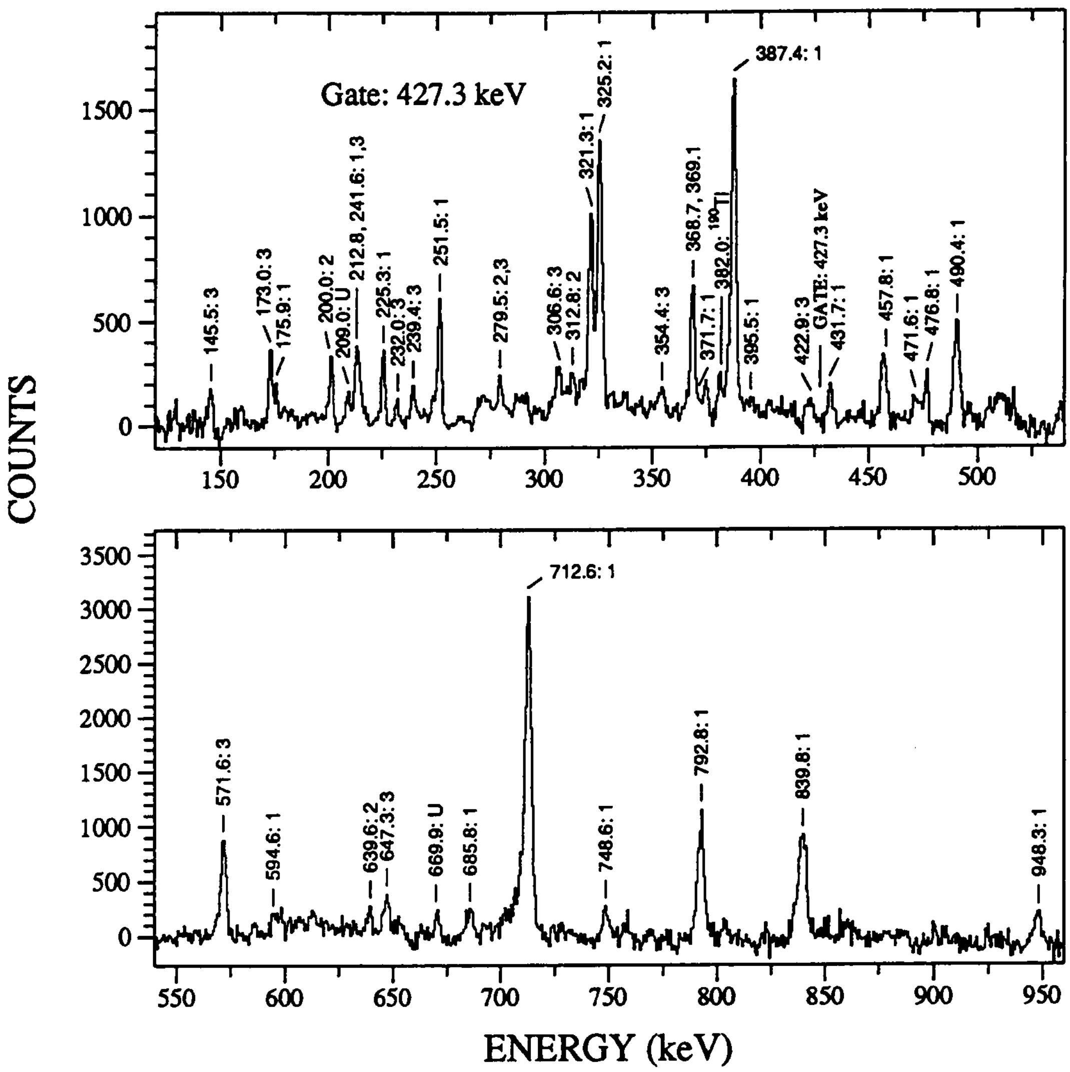

Figure 3.3: Efficiency corrected gate on 427.3 keV showing mostly transitions in Band 1. Due to the location of this gate in the level scheme, it contains members of all bands.

792.8 and 839.8 keV γ rays are. Using coincidence/anti-coincidence relationships like these, one can determine the placement of the 427.3 keV γ ray in relation to the others mentioned. For example, one sees a strong peak at 325.2 keV. An inspection of the 325.2 keV transition gate in Fig. 3.4 shows the 427.8 and 792.8 transitions, but not the 752.8 transition. Energy sums are an important criterion for the final placement. For example, when added together, 427.3 and 325.2 equal 752.5, which is very close to 752.8. Further, a look at the 752.8 gate shows neither the 427.3 nor 325.2 transitions. These facts used together give the relationship shown in the level scheme, *i.e.* that the 427.3 and 325.2 γ rays are in direct coincidence and are "bypassed" by the 752.8 γ ray.

Using bypasses to place transitions in the level scheme is a very useful tool, but is not foolproof. There are many times that two energies will accidentally add to equal another energy. Therefore, energy sums alone are not sufficient to fully determine the level scheme. The next item to consider is the DCO ratio. This ratio tells if a transition is of a quadrupole or dipole nature. A stretched dipole can only change spin by one unit, whereas a stretched quadrupole represents a $\Delta I = 2$ transition. This would mean that the crossover transition would need to be of a quadrupole nature and therefore an $E2$. This then would force the two transitions which were bypassed to have $\Delta I = 1$. Examination of the DCO ratios in Table 3.1 for the γ rays mentioned above shows that they meet these criteria. Most of the transitions in this level scheme were placed using this method, especially where a rotational behavior is exhibited.

Two common problems in level scheme building are doublets and self-gating transitions. Doublets are two transitions that have the same or nearly the same energy, such as those at 200.9 and at 321 keV. Self gating means that a transition appears in its own gate. This indicates that the transition is both a doublet and is in coincidence with itself. The 748 and 369 keV transitions are examples of this. Existence of these doublets can make placement difficult and requires comparison to gates on the nearby transitions. In addition to this, one can look at transitions that feed into the band and determine the relative intensities of the transition in

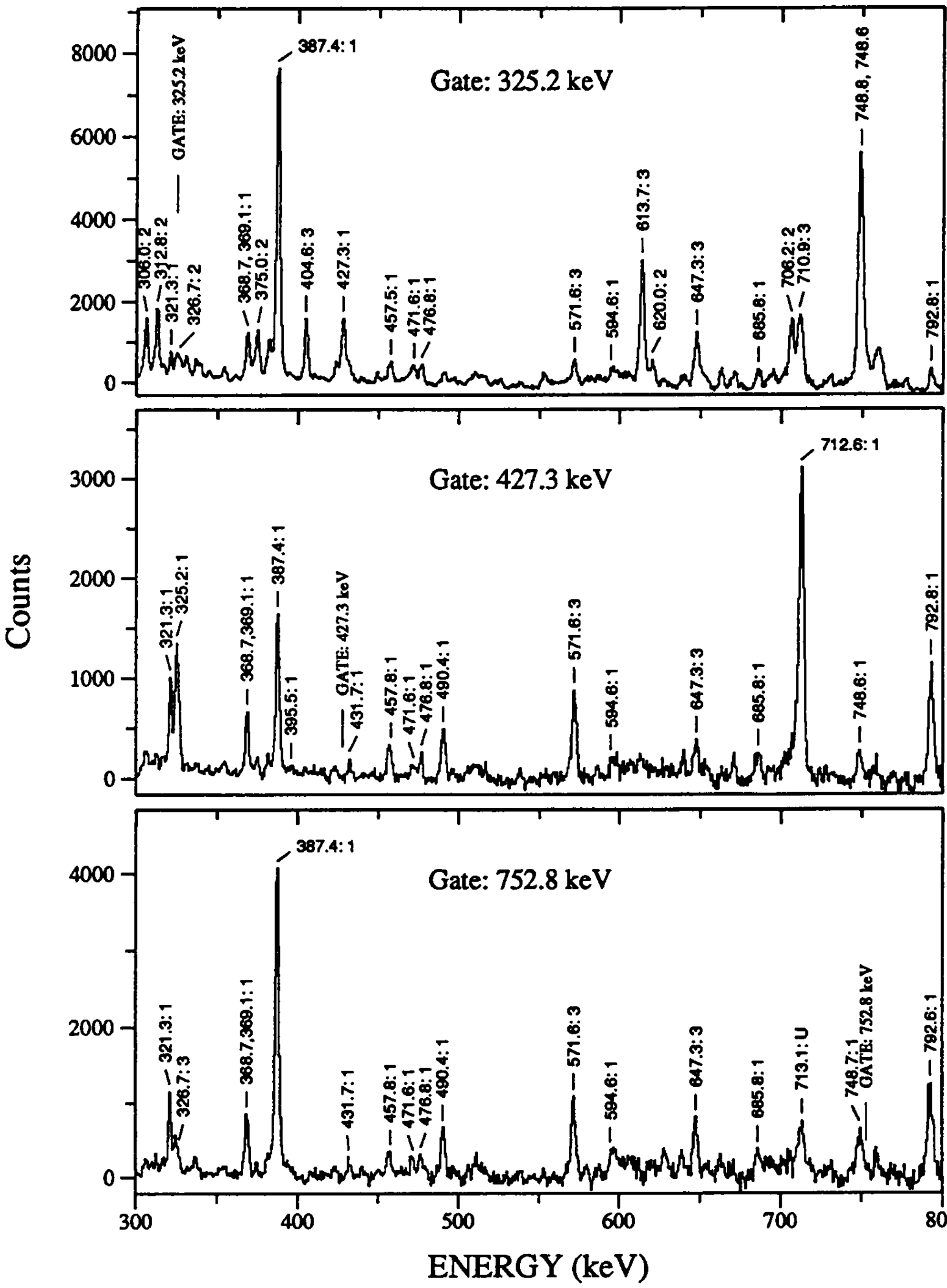

Figure 3.4: Efficiency corrected gates on 325.2, 427.3, 752.8 showing only a portion of the full-spectrum energy.

question. By doing this, one can see if the second member of the doublet is below or above the point where that feeding transition enters the band. Also, gating on one of the $M1$ transitions bypassed by the 748.8 γ ray (see Fig. 3.3) shows a transition near 748 keV but with not nearly enough intensity to be the 748.8 which feeds the $\frac{13}{2}^-$ level. Since there is no room left below the 748.8 it is evident that the other 748 is higher in the band. A similar method can be applied to the 369 keV transitions to lock them into place. Here one would actually gate on the $E2$ transitions which bypass the 369 line.

Especially in the case of doublets, it is good to have more than one check for the placements in the level scheme. One way to do this is with the level intensity balance discussed earlier. By comparing the intensity going into a level with that coming out, it is possible to determine if there is any surplus intensity which would have to be carried away by another decaying transition. These balances are given in Table 3.2. The negative balances mean that there is more intensity leaving a level than coming into it. This is a concern if the number is too large, but in general an imbalance of this type is natural and is caused by a perhaps large number of weak (and unseen) transitions feeding the level from above. However, for the imbalance at level 2301.5, this is not the case. There are 14.18 more units of intensity leaving the level than coming in. This could be partially explained by above feeding γ rays, especially since this level lies in the band crossing region. Also there could be a problem with the intensity of the 839.8 keV γ ray. Because of its relatively high energy, this peak is broad and difficult to fit. It also sits in a very cluttered region of the spectrum, so it is likely that some of the fault can be attributed to contaminants. Therefore it is possible that the reported intensity for the 839.8 keV transition is slightly too high, contributing to the negative imbalance at this level

Table 3.2: Level intensity balances. Positive values represent more intensity entering a level than leaving, negative values represent more intensity leaving a level than entering it.

Band	Energy	Int. In	Int. Out	In-Out
1	4731.0	5.10	26.64	-21.54
1	4267.0	15.60	16.92	-1.32
1	3895.3	26.19	25.67	0.52
1	3463.6	18.50	25.27	-6.77
1	3147.0	30.96	29.50	1.46
1	2778.3	32.40	32.50	-0.10
1	2553.0	33.36	35.36	-2.00
1	2301.5	46.82	61.00	-14.18
1	2088.1	14.88	14.97	-0.09
1	1932.8	10.03	20.05	-10.02
1	1630.3	10.50	17.44	-6.94
1	1461.2	64.50	57.66	6.84
1	1139.9	43.76	41.91	1.85
1	712.6	80.66	68.02	12.64
1	387.4	127.0	100.00	27.0
2	5131.0	2.15	3.75	-1.60
2	4776.5	3.75	10.33	-6.58
2	4493.6	5.00	5.20	-0.20
2	4214.1	10.53	13.02	-2.49
2	4024.9	23.35	$<$ 29.90	—
2	3824.0	$<$ 42.92	29.48	—
2	3664.4	25.14	28.46	-3.32
2	3375.3	22.11	42.56	-20.45
2	3044.7	25.72	37.67	-11.95
2	2669.7	45.46	30.97	14.49
2	2343.0	36.12	34.61	1.51
2	2030.2	41.32	50.31	-8.99

and subsequently the positive imbalance of 6.84 units at level 1461.2.

What really causes concern is when the imbalance is positive, which means that there is less intensity leaving the level than came in. This poses a problem because if the intensity is seen coming in, it has to go somewhere and therefore it should be possible to identify the transition(s) which would serve to carry it away. After a search is made and no such transition is found, it is likely that some of the individual

Table 3.2: (continued)

Band	Energy	Int. In	Int. Out	In-Out
3	3024.4	11.85	11.19	0.66
3	2832.1	6.13	—	—
3	2794.5	—	7.34	—
3	2656.6	5.07	9.33	-4.26
3	2583.7	—	10.27	—
3	2562.5	7.34	11.02	-3.68
3	2439.5	8.46	5.44	3.02
3	2377.1	9.33	17.62	-8.29
3	2323.1	11.02	14.58	-3.56
3	2187.5	8.31	18.62	-10.31
3	2132.9	10.66	12.68	-2.02
3	2108.5	22.41	30.57	-8.16
3	2022.0	17.87	23.26	-5.39
3	1884.7	99.12	93.96	5.16
3	1778.5	44.04	14.08	29.96
3	1711.7	51.78	83.48	-31.70
3	1405.7	42.52	43.77	-1.25
3	1001.1	89.04	87.74	1.30

intensities were incorrect. There are three levels in this band that fall into this category. At level 1461.2 there is an imbalance of +6.84 units. This could possibly be related to the 839.8 transition as discussed in the last paragraph. Another factor here could be that the 321.3 keV transition is a doublet whose other member is a transition in Band 3. The second imbalance of +12.64 units at level 712.6 could be related to the fact that 325.2 is close in energy to the 326.7 keV transition in Band 2. Most likely, however, it is due to the 918.5 keV γ ray which enters at the crossing. Although it fits here by coincidence relations, its intensity is somewhat suspect due to statistical inaccuracy because of its weakness. The third imbalance of +27.0 is at the 387.4 level. One reason for this could be that the intensity of the 613.7 transition feeding it from Band 3 is too high. This, in fact, seems to be the case. The 613.7 keV γ ray sits on a relatively broad neutron peak that is created by a reaction within the Ge detector. This "bump" is mainly caused by the excitation of the first excited state in the most abundant ^{74}Ge isotope (excitation energy of 595.9 keV with a lifetime of 18.1 ps [28]) through (n, n') scattering. A detailed description of this type of beam induced background in given in reference [29]. Great care was given to negate the effect of this bump, but still the intensity seems to be too high. Another explanation of this would be that the 613 keV transition is a doublet, but there seems to be no evidence of this. However, both of these possible explanations are complicated by the fact that the decay intensity balance at the 1001.1 keV level in Band 3 is very good, which would suggest that the intensity values for 613.7 are reliable. This imbalance for the 387.4 keV level is within 12% of the total feeding and decay intensity, which might just indicate the precision of this measurement.

With the exception of the cases mentioned, the level balances for this band fall within reason. Although possible reasons for the imbalances at levels 712.6 and 387.4 are offered above, they do not fully explain the imbalances. There seems to be something else complicating the intensities here, but it is neither seen nor understood at this time.

Finally, it can be seen that the DCO ratios for this band agree well with the spin and parity assignments. Exceptions are the 918.5 and 948.3 keV γ rays. From their placement in the level scheme, these should both be $\Delta I = 2$ transitions. The DCO ratios actually found, however, are more indicative of a $\Delta I = 1$ transition in each case. Again, since DCO ratios rely on a fitting of the area under the peak, this discrepancy is probably due to the difficulty of fitting these high energy peaks. Several attempts were made to get the "best" fit, but the results were the same. All in all, however, the features of this band seem to be very precisely established by energies, intensities and DCO ratios of the transitions involved.

Spin values for this band were derived starting with previous work [1, 2, 3] and using the DCO ratios to assign spins to the levels continuing up the band. In the case of the 1630.3 and 2088.1 keV levels the spins were determined using the 490.4, 457.8 and 212.8 keV transitions since the DCO ratios for the 918.5 and 948.3 keV transitions are ambiguous.

3.3 The $i_{13/2}{}^{+}$ Band (Band 2)

This band also exhibits a rotational-like structure presumably with a backbend at around a spin of $\frac{29}{2}^{+}$. As in Band 1, spin assignments were fairly straightforward using the DCO ratios. One interesting feature of this band is the missing $E2$ transitions above the "backbend region." Beyond this region in the level scheme, the intensity falls off too sharply for these to be seen. To support this idea, notice that the 390.4 and 564.1 keV transitions are also significantly weaker than the transitions below. While the reported intensity for the 390.4 keV transition of 13.0 units is not especially small, one has to take into account that the 390 keV transition is also a contaminant from ^{191}Hg [6] and it sits on the shoulder of the 387.4 keV transition in this nucleus. Therefore, it is likely that its actual intensity is less than 13 units. The two highest transitions in the band are placed in tentative order based on their intensities in gates lower in the band. There are no observed crossover $E2$ transitions to firmly establish their order.

A few level intensity imbalances are also in this band. The spaces at the 3824.0 and 4024.9 keV levels are left blank because the 200.9 keV γ ray is self-gating. Attempts to place the second 200.9 have proven useless and therefore it was impossible to conclude what part of the intensity of this multiplet belongs to the transition linking these two levels. Therefore, the intensity reported for this γ ray is actually the intensity of the multiplet and should be viewed as an inflated upper limit for the 200.9 keV line. Concerning the 3375.3 keV level, there is a large deficit of feeding intensity of –20.45 units. The intensity of the 449.0 keV transition is low, but this is in the band crossing region with presumably reduced $E2$ strength. Also, there are likely a number of weak unseen transitions feeding the 3375.3 keV level as a result of the sharp band crossing. The imbalance at the 2669.7 keV level of +14.49 units seems to suggest a missed decaying transition. A search has been made for such a transition but none was found. Another possibility could be related to the fact that the 326.7 keV transition is close in energy to that of 325.2 in Band 1. The two imbalances finally to be discussed for this band, -8.99 units for the 2030.2 keV level and –11.95 units for the 3044.7 keV level, do not pose any real problem. It is likely that there are other unseen transitions feeding the levels from above. Also, the transition leaving the 2030.2 keV level is a dipole with a relatively low energy of 145 keV. This means that it has a relatively high internal conversion coefficient. Thus, even a small error in the γ-ray intensity could make a large difference in the decay intensity.

A gate on the 312.8 keV transition is shown in Fig. 3.5. In this spectrum, one can clearly see Band 2 and its main decay pathway through the 145.5, 173.0, 306.0, 404.6, and 613.7 keV transitions of the other band, called Band 3. Although this gate is fairly clean, a few peaks appear here that are not placed in the level scheme but they are associated with this nucleus. Some of them are listed in Table 3.1 with a "U" (unplaced) as their band designation.

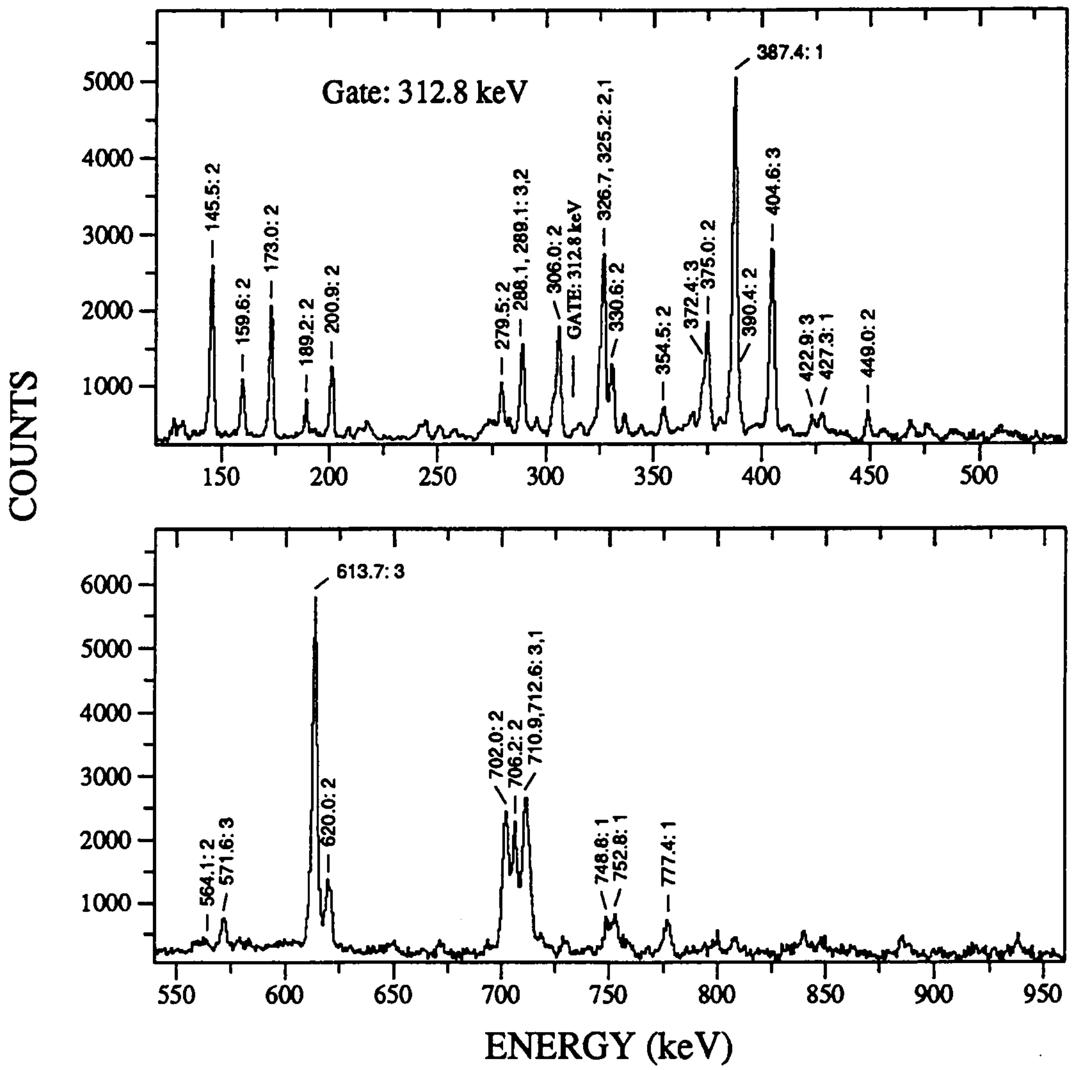

Figure 3.5: Efficiency corrected gate on the 312.8 keV transition in Band 2.

3.4 The Irregular Level Structures (Bands 3 and 3a)

This band is a good example of the usefulness of level intensity balances. While looking at the level balances during the process of building this level scheme, it was noticed that there was a considerable amount of surplus intensity feeding the 2343.0 level in Band 2. This prompted a search for a transition to carry that intensity away and led to the discovery of the 321.0 and 458.6 keV transitions originating at that level. Further investigation resulted in the development of Band 3. In contrast to Bands 1 and 2, this band shows no rotational-like structure, but more closely resembles irregular, single-particle like structure. An explanation for this structure will be discussed in Section 4.3. Besides solving intensity imbalances experienced in an earlier stage of this work, the presence of this band help resolve some problems which up to that point still existed, *e.g.* the placement of the 303.4 keV transition and the fact that the 306 keV γ ray is self-gating. It also gave a place for other γ rays that were recognized but previously unplaced.

Description of this structure is divided into two parts, one below the level of 1884.7 keV and the other above. The area below is very strong and provides the decay pathway for Band 2. This part was known previously and understood before the discovery of the upper part. The upper part is what is very new. Its main decay sequence involves the 137.3, 165.5, 303.4, 189.6, 279.5, 367.8, 272.0 keV transitions. A parallel sequence proceeds through the 354.4, 306.6, 144.2, 248.4, and 192.5 keV transitions. The final strong sequence begins at the 1461.2 level and consists of the 647.3, 214.6, 239.4, and 232.0 keV transitions. Other transitions in the band are weaker and serve to link the three main sequences together in a complicated fashion. A spectrum showing most of these lines is given in Fig. 3.6.

Assembly of this structure was not straightforward. The method of using bypasses as detailed earlier was not as useful here, but it was possible to add two or more transitions in a sequence and find a sum of two other γ rays to match that sum. Another complication was in the double nature of some of the γ rays. The 144.2 keV transition is close in energy to the 145.4; the 189, 192, 252, 279, 306, and 354 keV transitions are all doublets; 272.0 is one of the major transitions in ^{190}Tl

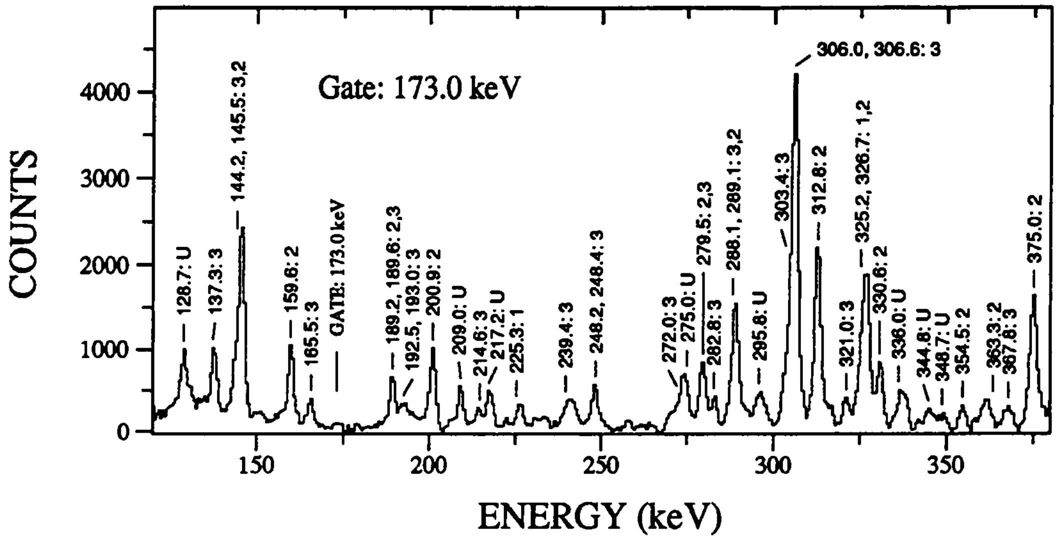

Figure 3.6: Efficiency corrected gate on 173.0 showing the main sequence and supporting lines of Band 3. Since this region of the level scheme is complicated, it is difficult to get a clean gate. Therefore, a gate on 173.0 is used, showing only the range of energies that appears in the upper part of band three.

and is seen as a contaminant in our data; and 165.5 keV is also a contaminant from ^{191}Hg. Careful gating and scrutiny of those spectra were the only way to extract these results.

Due to the weakness of many of these transitions is was also difficult to get reliable DCO ratios. Spin assignments are complicated and therefor rather tentative. Up to the 1884.7 keV level it was straightforward to assign spins as in the other bands. Above this, it was necessary to choose transitions with reliable DCO ratios on which to base a spin assignment. The first step was the 137.3 keV transition, which has a DCO ratio indicative of a stretched dipole assignment establishing the $\frac{21}{2}^+$ level. Above that, the 165 keV transition was too weak to yield a reliable ratio, so it was necessary to consider another pathway, *viz.* the 303.4 to 272.0 keV sequence. The DCO ratio of each transition in the sequence indicates a stretched dipole assignment which allows one to set the spins on those levels. As a check, the DCO ratios for the transitions in the 354.5 to 192.5 keV sequence indicate stretched dipoles, which gives spins equal to those just determined by the other sequence. In the third sequence, 647.3 to 232.0 keV, all transitions seem to be stretched dipole in character and thus give rise to the spins assigned there. None of these three sequences give spins that conflict with each other and in addition the assignments are compatible with the other connecting transitions in most cases. Possible exceptions to this clear consistency are the 2439.5 and 2187.5 keV levels. The 2439.5 keV level is tentatively assigned a spin of $\frac{21}{2}^+$, as is also the levels at 2187.5 and 2022.0 keV. The connecting lines are 252.0 and 165.5 keV, both of which are required to be dipoles of $\Delta I = 0$. However, the DCO ratio of the 165.5 keV transition is unobtainable and the ratio for 252.0 is difficult to extract in view of the strong 251.5 keV transition. These spins are given in parentheses in view of the uncertainties in the DCO ratios.

To check the assignments in this band we again apply the intensity imbalance test. Since many of these transitions are weak and members of a doublet, the balances have larger error bars. This by itself can account for some of the imbalances. The imbalances are mostly negative and are likely due to feeding from above that is too weak to be seen in this experiment. The missing assignments for the 2583.7 and 2832.1 keV levels are due to the fact that the 248 keV transitions are self gating so that their intensities could not be separated from each other. There is a positive imbalance of 3.0 units at level 2439.5. This could be due to a couple of factors. The low energy value of the feeding transition of 144.2 keV indicates a large internal conversion coefficient. Also the intensity of both decaying transitions may be a bit off since the 306 keV transition is a self-gating doublet and the 252 keV transition sits on the shoulder of an intense peak.

The other intensity imbalance is not so easily dismissed, and it consists of discrepancies at two levels. There is an imbalance of +29.96 units at the 1778.5 keV level and one of –31.7 units at the 1711.7 keV level. Similarly to the case of the 145.5 keV transition, the 106.6 keV transition is low in energy and exhibits a dipole nature, therefore its intensity could be suspect. However, the agreement in the above level (1884.7 keV) is very good and lends credence to the reported intensity value for the 106.6 line. This problem could be solved by a transition of 66.8 keV between the two out-of-balance levels. The transition would lie in the X-ray region and would be difficult to see. Due to its low energy, this transition would also be highly converted and, if it were a dipole, its coefficient would be around 31. Since it is thought that this transition must carry 30 units of decay intensity (this is roughly what is needed to correct the intensity imbalance), it would only need to have an I_γ of around 1%. The low detector efficiency at this energy and the threshold of the time discriminator also makes such a γ ray difficult to see. A search of the appropriate spectra gave no indication of a 1% intensity 66.8 keV γ ray. However, we postulate its existence in order to offer a solution to the intensity imbalances on the 1711.7 and 1778.5 keV levels.

CHAPTER 4

Discussion

4.1 Shape Coexistence

As mentioned in Chapter 1, the ground state of ^{191}Tl corresponds to having the valence proton in the $s_{1/2}$ orbital. This can be understood from the single-particle level diagram in Fig. 4.1. For this graph a deformed Woods-Saxon potential developed by the Warsaw group [30] is used to calculate the single-particle energies of the proton orbitals of interest (around $Z = 82$) as a function of the quadrupole deformation parameter β_2. Details of these standard calculations can be found, for example, in reference [31]. In general, this diagram can be used for both proton or neutron systems, since the effective potential wells for both kinds of particles are very similar. Since ^{191}Tl has an even number of neutrons and an odd number of protons, only the proton orbitals will be discussed, because it is the unpaired or odd particle that determines the spins and parities of the bandheads. Each line in the figure represents a proton configuration and can account for two particles, one spin up and one spin down. The Y-axis gives the level energy in MeV and the X-axis corresponds to β_2. The circled numbers are proton particle numbers, Z, and are placed to indicate significant energy gaps between the filled and unfilled levels. At $\beta_2 = 0$ these numbers correspond to closed shells and thus give the nuclear magic numbers. Two different types of lines are used to indicate the parity of the shell from which they originate, with a solid line being positive parity and a dashed line negative parity. Each line is also labeled with its asymptotic quantum numbers (Nilsson quantum numbers) enclosed in square brackets followed by the K value for

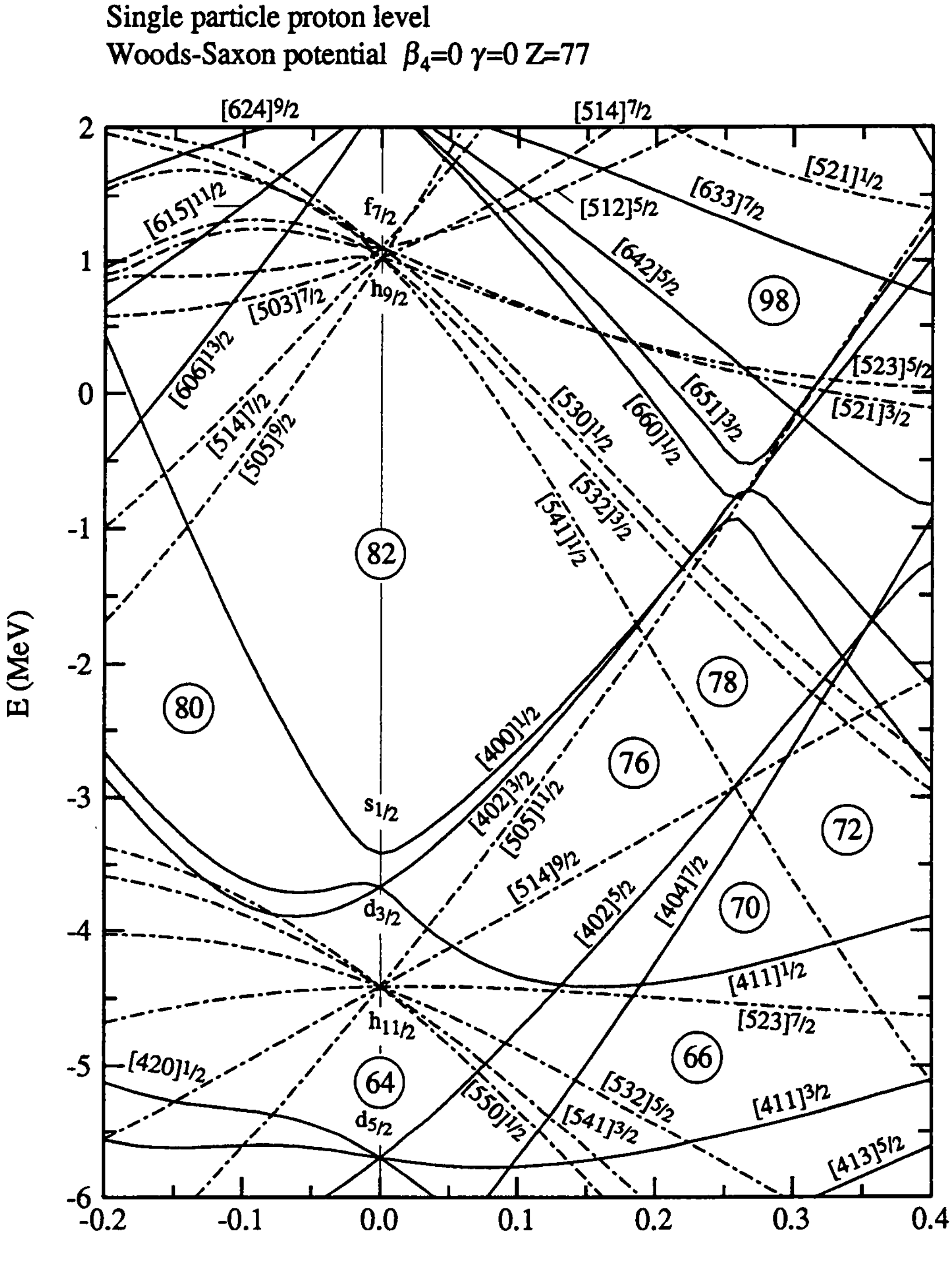

Figure 4.1: Proton single particle levels as a function of β_2 deformation calculated using the Woods-Saxon potential [30,31].

the orbital, which is the projection of the total angular momentum onto the nuclear symmetry axis.

The plot of single-particle energy levels ranges from negative to positive values of β_2, zero indicating a spherical nucleus. As one moves away from $\beta_2 = 0$, the nucleus becomes deformed. A positive β_2 would be of a prolate shape (pointed at the poles like a lemon) and negative values would be oblate (flattened at the poles like an orange). At the spherical $\beta_2 = 0$ line the various orbitals for each shell state are degenerate in energy, but as the nucleus deforms in either the prolate or the oblate direction, this degeneracy breaks down and gives rise to the single-particle orbitals corresponding to different projections of the single-particle angular momentum on the nuclear symmetry axis. Some of these lines are relatively flat, but most have some slope to them. It is this slope that indicates the "shape driving" nature of that orbital. For instance the $s_{1/2}$ $[400]\frac{1}{2}$ orbital looks somewhat like a upturned parabola centered at $\beta_2 = 0$; therefore, if this orbital were occupied by the odd particle, it would be energetically favorable for the nucleus to be spherical, hence this orbital drives the nucleus to be a sphere. On the other hand, the $h_{9/2}$ $[541]\frac{1}{2}$ orbital just above this one is prolate driving due to its slope.

The Woods-Saxon diagram can be used to predict the configurations behind the structures seen in ^{191}Tl. This nucleus has 81 protons, so the ground state would fall just below the $N = 82$ gap, putting the 81^{st} proton into the $s_{1/2}$ $[400]\frac{1}{2}$ orbital which, as we noted before, is spherical. The nucleus is formed in the experiment with a large amount of angular momentum, is rotating quite rapidly and would be expected to be deformed, at least at high excitation energies. The neighboring nuclei all indicate that ^{191}Tl will have a somewhat oblate shape at low excitation energies, and that can also be seen from the diagram with some knowledge of the level scheme. Both rotational bands in ^{191}Tl are strongly coupled, meaning that the rotational levels are ordered by increasing spin with both signatures present, connected by $E2$ and $M1$ transitions. This is a characteristic of populating high K orbitals, whereas bands built on low K orbitals are mostly decoupled. Looking at the diagram, one can see that the orbitals on the prolate side lowest in energy for each subshell have low K values. On the oblate side, however, the lower energy orbitals for each subshell have high K values. The observation of strongly coupled bands in ^{191}Tl is thus a strong indication that this nucleus is oblately deformed.

The extent to which a nucleus is deformed can be estimated using methods that will be detailed in Section 4.2 which give the values of $\beta_2 = -0.15$ and -0.19 for Bands 1 and 2 respectively. These lines are marked on the diagram for purposes of discussion, their origin will be discussed in Section 4.2. At $\beta_2 = 0$, the $s_{1/2}$ $[400]\frac{1}{2}$ orbital is obviously preferred. However, as one moves toward larger oblate deformation, the $s_{1/2}$ orbital climbs higher in energy whereas the $h_{9/2}$ $[505]\frac{9}{2}$ orbital drops lower in energy and is in fact lower than $s_{1/2}$ $[400]\frac{1}{2}$ at $\beta_2 = -0.15$. This means that at higher oblate deformation it is possible to populate the $h_{9/2}$ $[505]\frac{9}{2}$ orbital, which is the assignment for Band 1. Band 2 is considered to be built on the $i_{13/2}$ orbital, which would seem unlikely at first because at $\beta_2 = 0$, the $i_{13/2}$ shell states are much too high in energy and particle number, and in fact are off the scale of the plot. However as one moves to larger oblate deformation, this orbital drops dramatically to an energy that is possible to be populated in this nucleus. This $i_{13/2}$ orbital is called an "intruder state" because it drops in from high above and is thus able to be populated in a mass region wherein it would normally be unreachable.

4.2 Total Routhian Surfaces

The rotating nucleus can be viewed from two reference systems, either the laboratory frame or the rotating (intrinsic) frame. When viewed from the intrinsic frame, the energy of the a single nuclear level with the rotational component removed is known as the routhian energy. For describing the shape of the nucleus when rapidly rotating, the Total Routhian Surfaces (TRS) are perhaps most useful. Often the TRSs are calculated using the deformation self-consistent Strutinski-Bogolyubov cranking approach with a non-axial potential as first presented by Dudek [32]. Calculations of this type are used in this work. These have been performed by Wyss *et al.* [33] for four different mass regions using a Woods-Saxon potential with appropriate parameters. Deformation parameters β_2, γ, and β_4 are obtained by minimizing the total routhians. That is, the local minimum of the TRS corresponds to the nuclear equilibrium shape for the configuration under consideration.

For the region around nuclear mass 180, the results of the TRS calculations are organized in the so called "Pt-mesh" and cover a deformation space of $\beta_2 \cos(\gamma + 30°)$ from 0.05 to 0.45 and $\beta_2 \sin(\gamma + 30°)$ from –0.20 to 0.30 over a rotational frequency range ($\hbar\omega$) of 0.0 to 0.6 MeV. From this mesh, plots like the one in Fig. 4.2 are made. The display shows a polar coordinate system with the radius lines giving the angle γ, and the concentric circles giving the quadrupole deformation parameter β_2. The angle γ is a "triaxiality parameter" related to the principle axes available for collective rotation. The value $\gamma = 0°$ represents the collective prolate, and the value $\gamma = -60°$ the collective oblate modes in the Lund convention [34]. Outside the collective sector, $\gamma = 60°$ and $-120°$ are the limits representing oblate and prolate non-collective (single-particle like) modes respectively. The results of these calculations have been explored for many configurations in ^{191}Tl in order to accurately describe the deformation.

Fig. 4.2 shows a TRS plot for the negative parity configuration for ^{191}Tl. In the first panel it is obvious that there is a minimum at $\beta_2 \approx 0.15$, $\gamma \approx -57°$. As $\hbar\omega$ increases, this minimum remains up to high rotational frequency. A second minimum develops at relatively low $\hbar\omega$, remains stable, and actually becomes the stronger of the two at higher frequency. The values $\gamma \approx -77.5°$ and $\beta_2 \approx 0.06$ indicate that this minimum is only weakly deformed and rather associated with a spherical shape. The minimum at larger deformation is related to the $\pi h_{9/2}$ configuration which is responsible for Band 1 in the level scheme (Fig. 3.1). The nearly spherical minimum has a more complicated nature and is likely related to Band 3. This relationship will be discussed in Section 4.3.

The positive-parity configuration is shown in Fig. 4.3. A similar situation is seen here at low frequency with a weakly deformed minimum ($\beta_2 \approx 0.08$, $\gamma \approx -56°$) that remains stable to high $\hbar\omega$ values, and the development of a second minimum ($\beta_2 \approx 0.19$, $\gamma \approx -52°$) at higher frequency. The difference here is that the lower deformation minimum comes at a lower rotational frequency than does the higher deformation minimum. This higher deformation minimum corresponds to the $\pi i_{13/2}$ configuration that is responsible for Band 2. Since it comes at higher $\hbar\omega$, the nucleus has developed more angular momentum by the time this minimum has formed. This could be one of the reasons that the rotational $i_{13/2}$ band does not begin at a level with a spin of $\frac{13}{2}^+$, but in fact has an origin at $\frac{21}{2}^+$. The first minimum of the positive parity configuration is essentially spherical and is most likely related to Band 3. Note that for both parities a superdeformed prolate minimum with $\beta_2 \approx 0.45$ is present in the TRS diagram and has been observed experimentally [13].

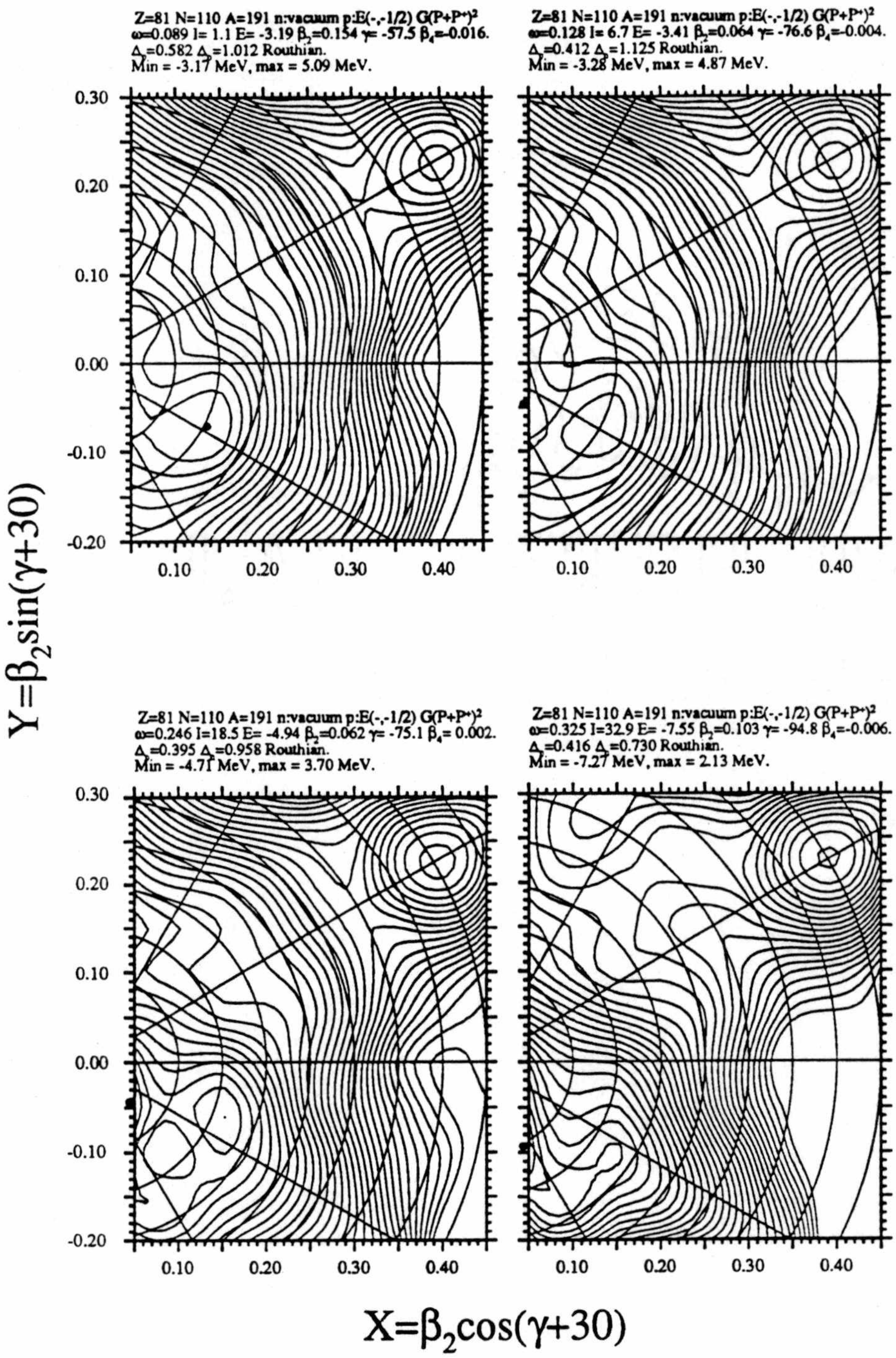

Figure 4.2: TRS plot for the negative parity configurations in ^{191}Tl using $\hbar\omega$ = 0.089, 0.128, 0.246, 0.325 MeV.

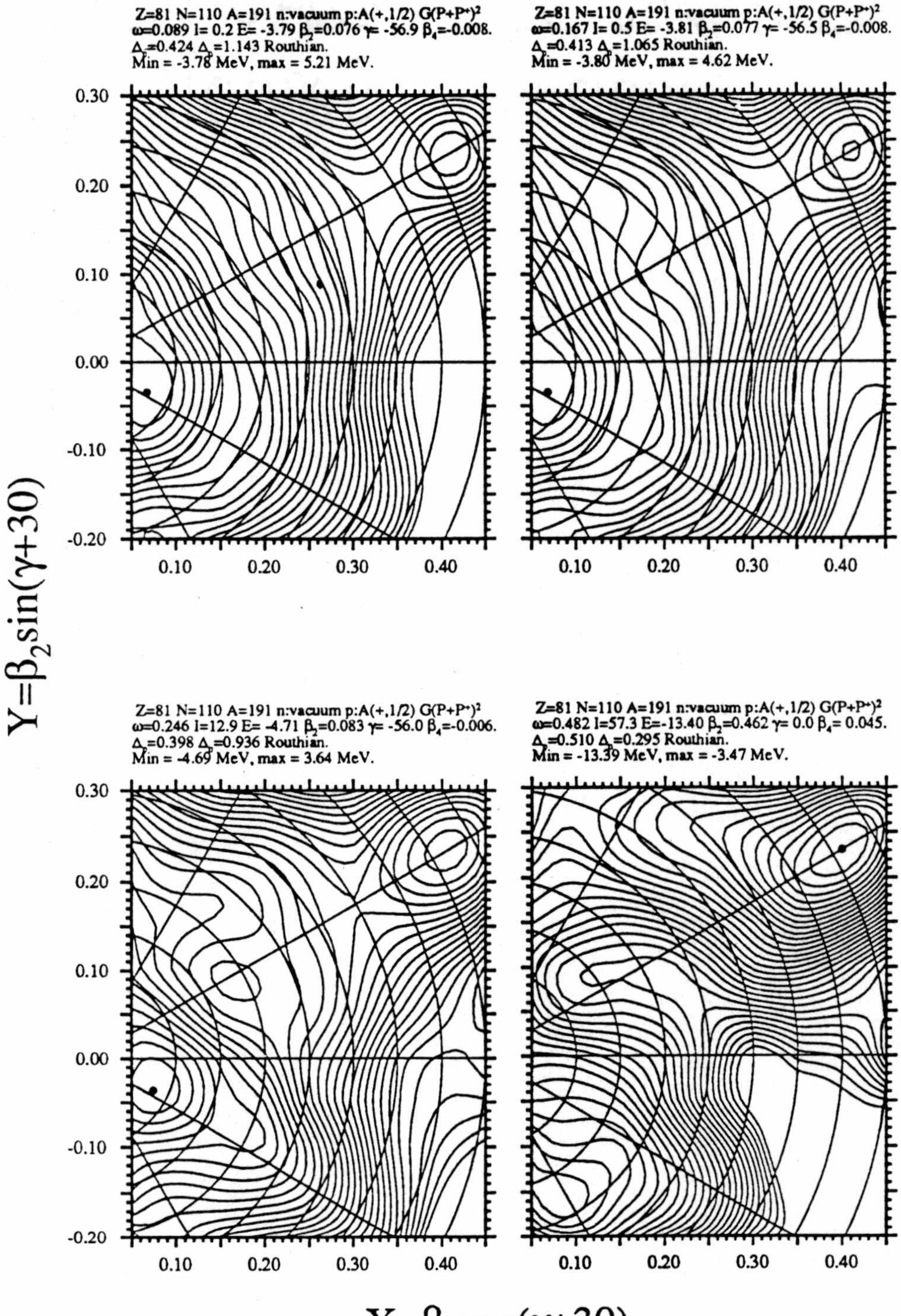

Figure 4.3: TRS plot for the positive parity configurations in ^{191}Tl using $\hbar\omega$ = 0.089, 0.167, 0.246, 0.482 MeV.

4.3 Coupling Schemes for the Irregular Level Structures

Systematics of neighboring nuclei and TRS predictions have served well to explain Bands 1 and 2 as rotational bands built on the expected proton configurations. Band 3, however, built on ${i_{13/2}}^+$, is of a different nature. It shows no rotational-like $E_\gamma(I)$ behavior, and is dominated by dipole transitions. Therefore, this structure seems to be more single-particle like, which would imply a spherical configuration. To explain the origin of such a configuration, we turn attention to the idea of coupling the shell states of this nucleus to the core states of an essentially non-deformed even-even neighbor. One possibility is to couple a single-particle hole to levels in ^{192}Pb. To do this one takes each shell state in ^{191}Tl ($s_{1/2}$, $h_{9/2}$, $d_{3/2}$, $i_{13/2}$) and couples it to each level in ^{192}Pb [35]. This is shown pictorially in Fig. 4.4 for the $h_{9/2}$ and $i_{13/2}$ states in ^{191}Tl. The $s_{1/2}$ and $d_{3/2}$ states do not give high enough spin values which match to the levels identified in structure 3, and are thus omitted from the graph. Each new level has an energy that is the value of the original level energy in ^{191}Tl plus the energy of the level in ^{192}Pb to which it is coupled. The spin range for each new level is obtained by vectorially adding the spins of each corresponding level in ^{192}Pb to the spin of the level being coupled to in ^{191}Tl. The result is a new set of levels for each coupling that has the same spacing as the original levels in ^{192}Pb but are offset by the energy of the ^{191}Tl shell state to which that level was coupled. Each of these new levels represents a multiplet of states that are degenerate in energy spanning the given spin range.

Having found these new levels, one then proceeds to match each level in Band 3 to one of the states in this new scheme. The results of this are shown in Fig. 4.5. Each spin value in a multiplet can only be used once, and it is necessary to match the

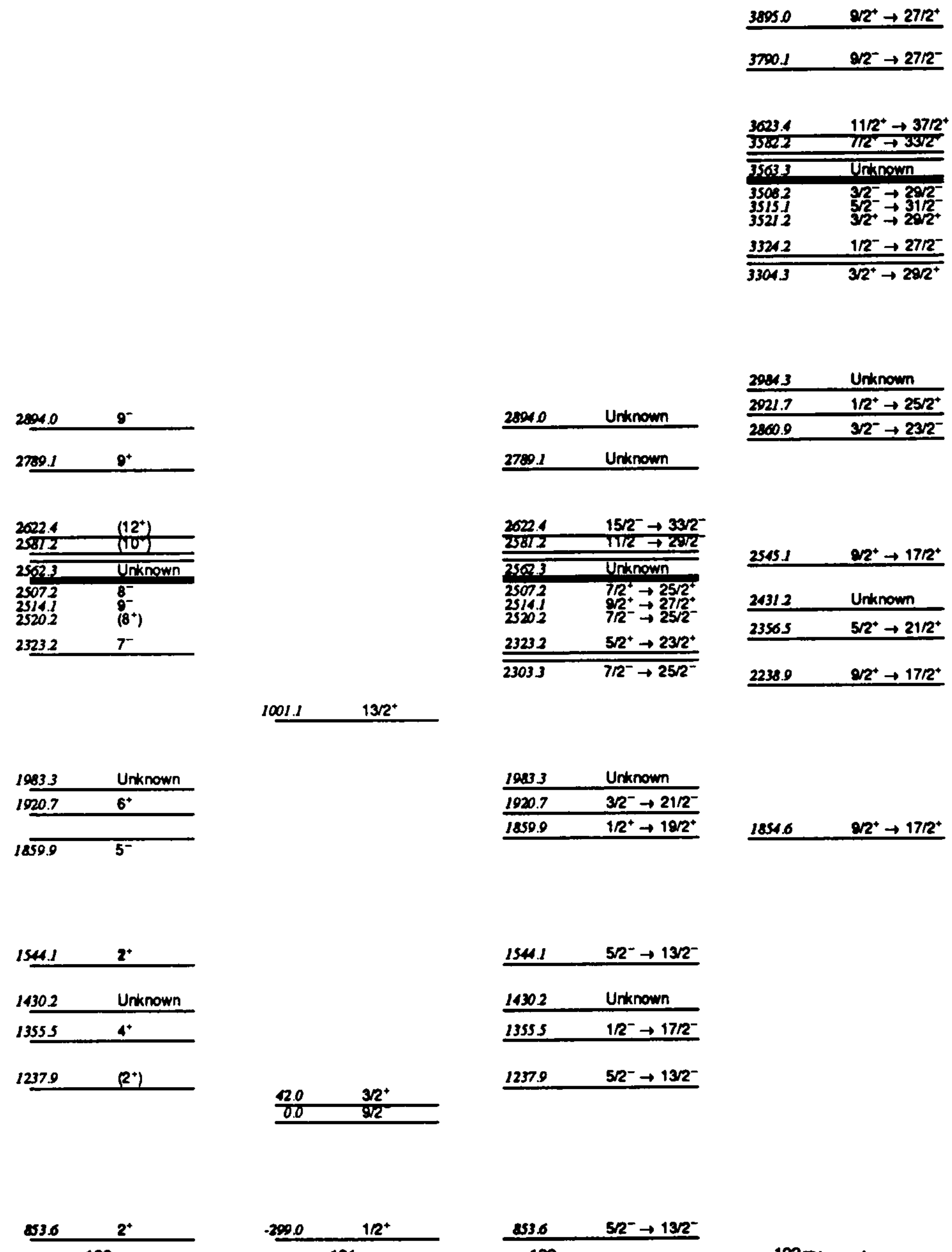

Figure 4.4: Coupling of spherical ^{192}Pb states [35] with the shell states of ^{191}Tl. Only the $h_{9/2}$ and $i_{13/2}$ states of ^{191}Tl are shown.

parity also. In some cases there is more than one way to connect the experimental states to the new scheme, and some of the spins for levels in ^{192}Pb are unknown, rendering these levels unusable, therefore some license is exercised. If these spins were known, it might be the case that some of the lower energy levels would have high enough spin to be useful. In all cases, however, the experimentally observed level is matched to the lowest energy theoretical level with known available spin.

This comparison produces some interesting results. First, the 2108.5, 2323.1, 2562.5 and 2794.5 keV levels in Band 3A can all be linked with the same multiplet (^{192}Pb(8^+) + $h_{9/2}$) in the coupling scheme. This supports the assigned parity and relates this structure more strongly with Band 1 as is indicated from gated spectra and the ^{191}Tl level scheme in Fig. 3.1. Secondly, the 1711.7 and 1884.7 keV levels are matched with the multiplet due to the ^{192}Pb(5^-) + $h_{9/2}$ coupling. These are the only other two levels that have direct transitions to Band 1. Furthermore, levels at 1405.7 and 1778.7 keV are shown matched with the ^{192}Pb(2^+) + $i_{13/2}$ and have no direct transitions to Band 1. These levels support transitions which carry most of the intensity from Band 2, so it is proper that they should be more strongly associated with the $i_{13/2}$ structure.

These experimental levels matched to the ^{192}Pb + $h_{9/2}$ couplings are nearly symmetrically spaced in energy about the calculated value for the degenerate multiplet. This is the type of behavior expected when the degeneracy of a multiplet is broken. This does not happen for the levels matched to couplings of ^{192}Pb + $i_{13/2}$. However, a definite trend is seen here with all of the experimentally observed states being matched to coupled multiplets that are consistently higher in energy.

In addition to giving an origin to each level in Band 3, this scenario helps to explain the proliferation of levels with like spins as describing members of separate

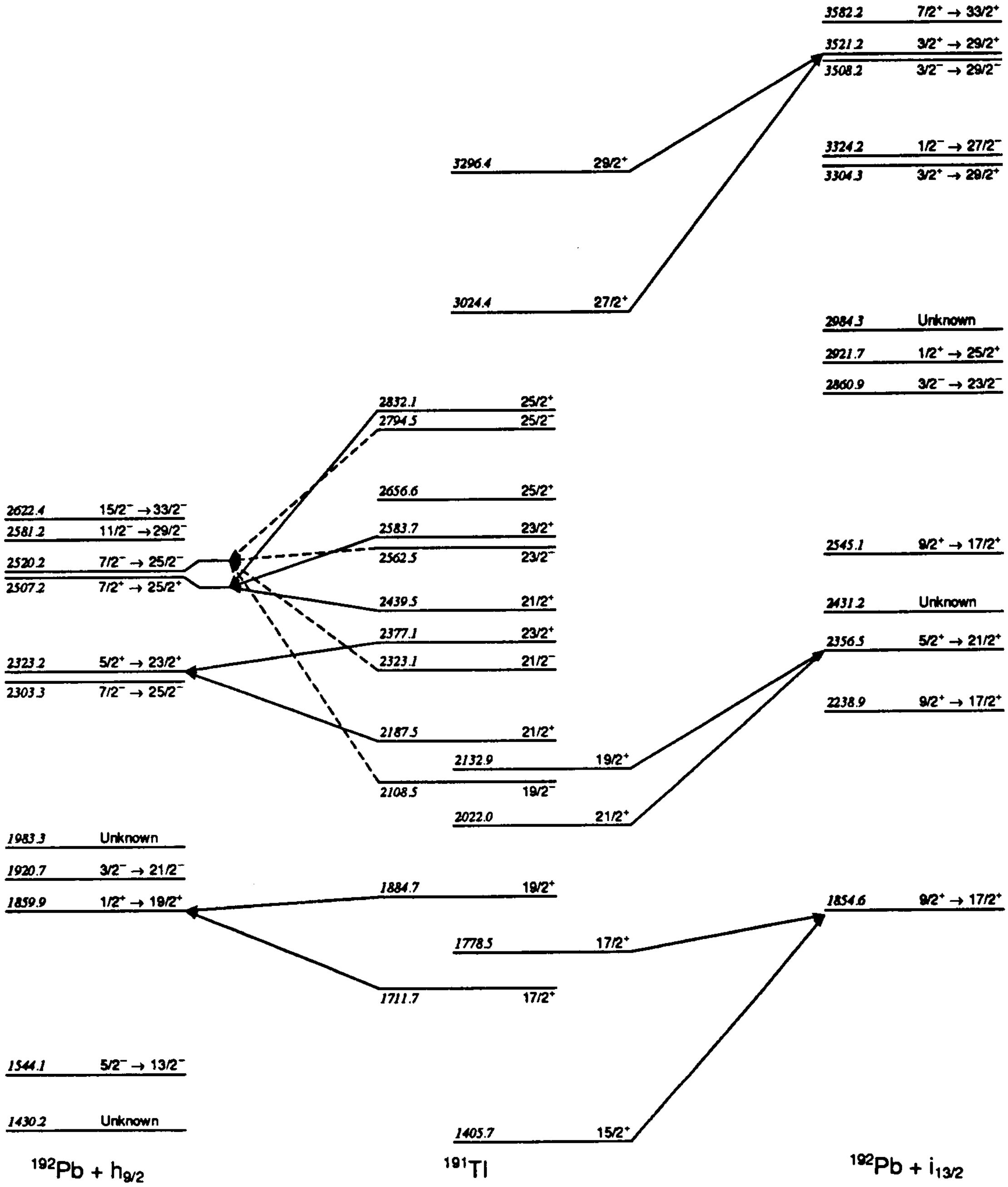

Figure 4.5: Matching of the levels of Band 3 in ^{191}Tl to the appropriate levels in the coupled scheme.

multiplets. The previous discussion helps to find an explanation for the 571.6, 422.6, and 647.3 keV transitions which link Bands 3 and 3a with Band 1 by showing that they are related to this negative parity structure through the couplings.

It is interesting to note that the $i_{13/2}{}^{+}$ state at the bottom of level structure 3 as well as the analog state in ^{193}Tl was proposed twenty years ago to originate from a well deformed oblate $\pi i_{13/2}$ [606] [5]. In a recent work on ^{193}Tl, a different interpretation for the $i_{13/2}$ state and the levels above in that nucleus has been favored, namely a single-particle-like excitation [11]. There is to some extent agreement between the present work and reference [11]. However, the important new information from this work is the observation of Band 2, which seems to be the expected $\pi i_{13/2}$ oblate deformed structure, although present at a significantly higher excitation energy than expected.

4.4 Rotational Alignment

So far, only proton configurations have been discussed. Although protons are responsible for the particular configurations observed, neutrons also play a role. For ^{191}Tl, the valence neutron shell is $\nu i_{13/2}$. Since there is an even number of neutrons and each orbital can hold only a pair of particles in time reversed (one spin up, one spin down) orbits, this orbital is full. As the nucleus begins to rotate at higher $\hbar\omega$, the coriolis force increases. At a critical angular momentum, this force becomes strong enough to cause one pair of valence neutrons to become unpaired and align with the rotational axis. The associated change in the moment of inertia ($\mathcal{J}$) of the nucleus, known as a band crossing, is expected to be evidenced experimentally by an irregularity in the E_γ vs. I behavior of the $E2$ sequence. In Band 1, for example, the $E2$ energies increase smoothly with spin, up to $I = \frac{19}{2}^-$, after which the $E2$ transition energy drops and again continues to increase smoothly with spin. This is caused by the alignment of a pair of $i_{13/2}$ neutrons. A similar situation is seen in Band 2 at a spin of around $\frac{33}{2}^+$.

Once the spins and transition energies are known, a total aligned angular momentum plot (Fig. 4.6) can be constructed from the experimental results. In this plot the aligned angular momentum is defined as:

$$i = I_x - I_{ref} \tag{4.1}$$

for an $I + 1 \rightarrow I - 1$ transition of energy E_γ. I_x describes the projection of the total angular momentum on the rotational axis and is given by $[(I + 1/2)^2 - K^2]^{1/2}$. The I_{ref} describes the angular momentum of the rotating core and is related to the rotational frequency by

$$I_x = \mathcal{J}\omega = (\mathcal{J}_0 + \mathcal{J}_1\omega^2)\omega. \tag{4.2}$$

The description for the moment of inertia $\mathcal{J}_0\hbar^2/\text{MeV}$ and $\mathcal{J}_1\hbar^4/\text{MeV}^3$ in equation 4.2 is called the Harris parameterization [36]. The Harris parameters $\mathcal{J}_0$ and $\mathcal{J}_1$ are chosen to fit the moment of inertia of the ground-state band of the "core nucleus," in this case, ^{190}Hg. The rotational frequency is half the transition energy for a $K = 0$ band, and generally is defined as:

$$\hbar\omega = \frac{dE}{dI_x} = \frac{\mathcal{J}(I+1) - \mathcal{J}(I-1)}{I_x(I+1) - I_x(I-1)}. \tag{4.3}$$

The "back bending" is caused by the neutron alignment, and the frequency in the middle of the backbend is known as the "crossing frequency" ($\hbar\omega_c$). This is an important parameter because there is no way to measure deformation directly via the experiments described here, and $\hbar\omega_c$ is a rough gauge of deformation. It is

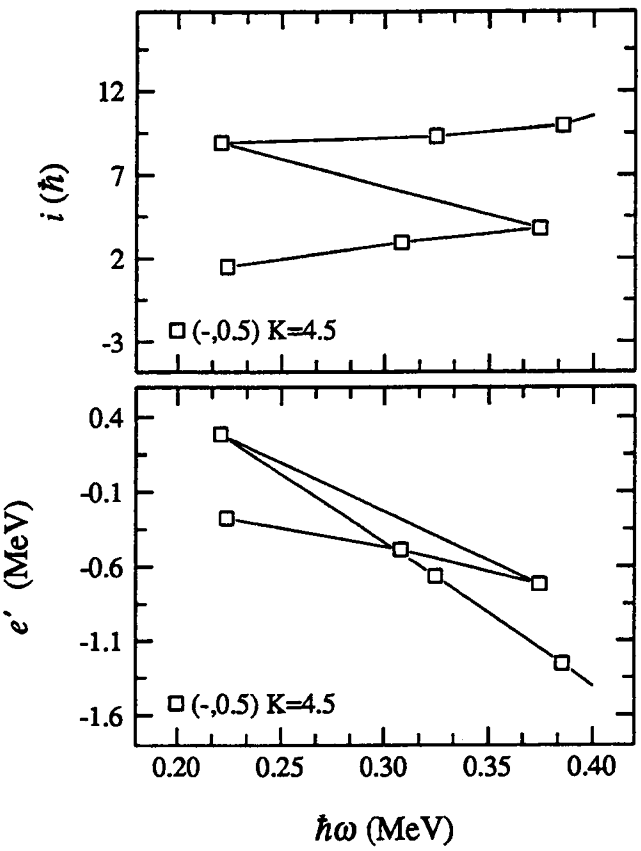

Figure 4.6: Top: aligned angular momentum for the favored signature of the $h_{9/2}$ band in ^{191}Tl, plotted versus rotational frequency. Bottom: the routhian for the same configuration. For both, a rotating reference is subtracted using parameters $\mathcal{J}_0 = 8$ and $\mathcal{J}_1 = 40$.

difficult, however, to extract a reliable value for $\hbar\omega_c$ from this type of plot because the definition of "middle" is subjective. A better way is to use the routhian energies. As stated before, these are the energies in the rotating frame, given in Fig. 4.6. The routhian is defined as

$$E' = E - \omega I_x. \tag{4.4}$$

As with aligned angular momentum, an energy of the rotating core is subtracted to give the quasiparticle routhian

$$e' = E' - E_{ref} \tag{4.5}$$

where

$$E'_{ref} = \frac{\omega^2}{2}\mathcal{J}_0 - \frac{\omega^4}{4}\mathcal{J}_1 - \frac{1}{8\mathcal{J}}. \tag{4.6}$$

In this case the routhian for the one quasiparticle band crosses that for the three quasiparticle at the crossing frequency, making it easier to extract a value.

Another way to view ^{191}Tl is as a proton coupled to a ^{190}Hg core. Fig. 4.7 shows aligned angular momentum plots of the rotational bands in ^{191}Tl compared to the ^{190}Hg core and the analogous bands in ^{193}Tl [11] compared to their ^{192}Hg [6] core. For all three structures in each group, the band crossing is caused by the alignment of a pair of $i_{13/2}$ neutrons, so they should all have nearly the same crossing frequency. Routhians were plotted for each of these structures in order to find their crossing frequencies. These values for $\hbar\omega_c$ are given in Table 4.1 along with their corresponding β_2 values which were extracted from TRS plots. It is evident that $\hbar\omega_c$ is not the same for each of these bands. It is important to note, however, that the deformations are different, and in both cases, the bands in the Tl nuclei are calculated to have larger deformation than their respective Hg cores and γ values

Table 4.1: Experimental crossing frequencies ($\hbar\omega_c$) for ^{191}Tl and ^{193}Tl, extracted from the data shown in Fig. 4.7. The β_2 values are extracted from TRS calculations.

	^{191}Tl			^{193}Tl		
	$i_{13/2}$	$h_{9/2}$	^{190}Hg	$i_{13/2}$	$h_{9/2}$	^{192}Hg
β_2(TRS)	−0.19	−0.15	−0.145	—	−0.15	−0.141
$\hbar\omega_c$(MeV)	0.24	0.30	0.22	0.22	0.28	0.21

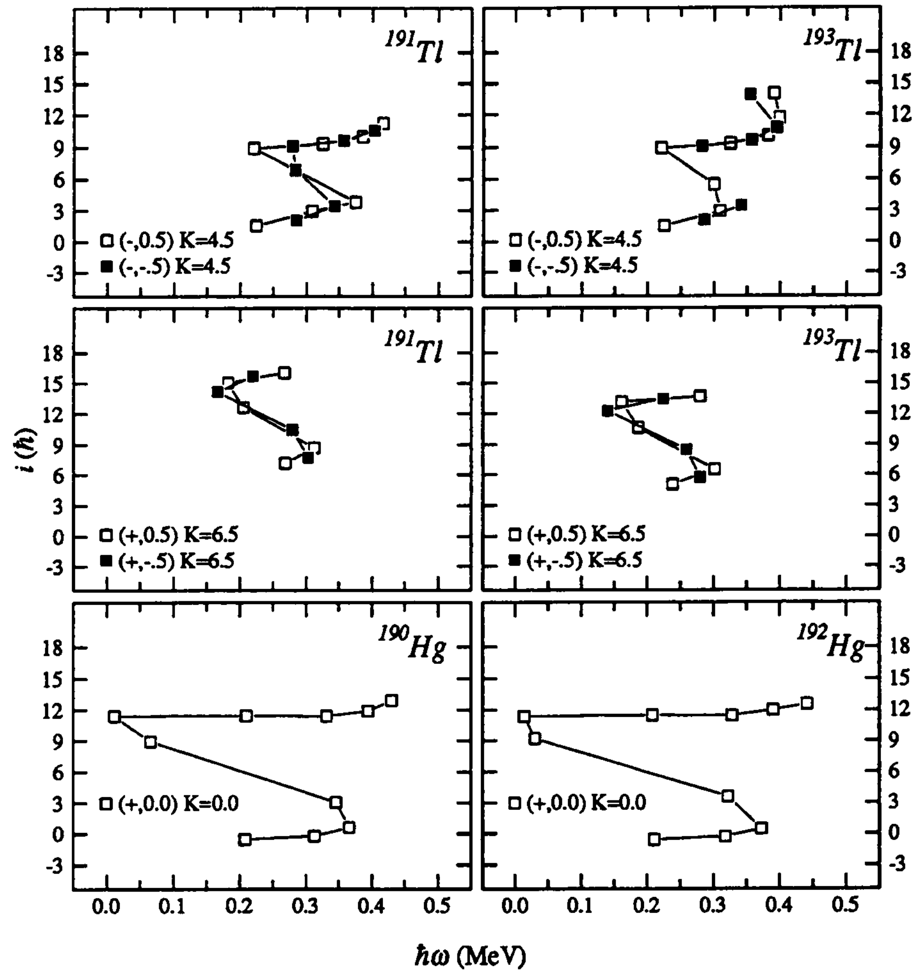

Figure 4.7: Aligned angular momenta versus rotational frequency for the $h_{9/2}$ and $i_{13/2}$ bands in ^{191}Tl and ^{193}Tl [11], and in the ground bands of the core nuclei [6].

that differ somewhat from the oblate axis (γ= -60°) used in the calculations.

To attempt to understand this dependency of $\hbar\omega_c$ on quadrupole deformation, we calculated the theoretical single-neutron routhians to obtain the crossing frequency using different values of β_2 and a fixed $\gamma = -60°$ to indicate an oblate shape. The Cranked Shell Model (CSM) code is used to calculate the quasi-neutron energies in a rotating Woods-Saxon potential as a function of $\hbar\omega$ [31]. The parameters for this calculation are deformation (β_2, β_4, γ), pairing gap (chosen from the BCS approach and is close to the odd-even mass difference), and Fermi level (chosen to give the correct number of neutrons). The results of this are shown in Fig. 4.8 and, although the trend is small, one can see that nuclei with larger β_2 should have lower values for $\hbar\omega_c$. When this theoretical result is applied to the crossing frequencies and deformation summarized in Table 4.1, some interesting observations can be made. Within the nucleus, either ^{191}Tl or ^{193}Tl, the expected trend is seen, that the larger deformation for the $i_{13/2}$ band compared to the $h_{9/2}$ results in a smaller $\nu i_{13/2}$ crossing frequency:

$$\beta_2(h_{9/2}) < \beta_2(i_{13/2}) \rightarrow \hbar\omega_c(h_{9/2}) > \hbar\omega_c(i_{13/2}). \tag{4.7}$$

This measured trend in crossing frequencies in ^{191}Tl and in ^{193}Tl does seem to validate the theoretical prediction of the deformation differences between $\pi h_{9/2}$ and $\pi i_{13/2}$.

However this general agreement for the two bands in ^{191}Tl and ^{193}Tl does not hold true for the core nucleus in either case, as the TRS calculations indicate that the deformation for ^{190}Hg is less than that for either band in ^{191}Tl, which should result in a higher crossing frequency than for either band in ^{191}Tl. In fact, the crossing frequency is lower in each Hg case than in the Tl bands. The reasons for the discrepancy are not clear, although it is likely that the effects of the other deformation parameters (β_4 and γ) are significant. The TRS calculations indicate rather similar values of β_4 and γ for the configurations described here, but perhaps there are larger differences. Likewise, the deformation changes (β_2, β_4, or γ) between zero and two quasiparticle bands in ^{190}Hg, for example, may be much more significant than between the one and three quasiparticle structures in ^{191}Tl. Such a change would certainly need to be carefully included in the CSM calculation.

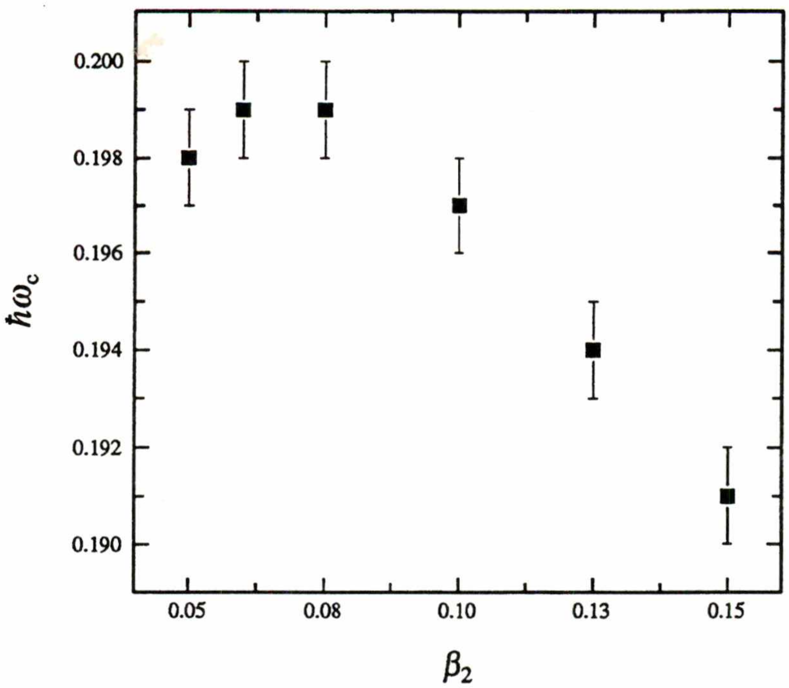

Figure 4.8: Theoretical crossing frequency, $\hbar\omega_c$, as a function of β_2 deformation.

In general, for a smaller deformation the moment of inertia is expected to be smaller due to the relationship

$$\mathcal{J} = \left[\frac{\beta Z A^{1/3}}{114 \pm 8}\right]^2 (\mathrm{MeV}^{-1}\hbar^2) \tag{4.8}$$

given in reference [38]. Consequently, the coriolis force ($\propto (I \cdot j)/\mathcal{J}$) should be larger and the crossing should appear at lower frequency.

CHAPTER 5

Conclusions

5.1 Present Work

This work used heavy-ion induced nuclear reactions to study high-spin levels in ^{191}Tl. Three experiments were performed using three different multi-detector arrays of γ-ray detectors at Oak Ridge National Laboratory and Argonne National Laboratory. The data from these experiments enabled the discovery of two superdeformed bands in the nucleus [13]. Since these superdeformed bands lie high in energy and are weakly populated, it was necessary to collect a large amount of data. This situation permitted a detailed analysis of the normally deformed states in ^{191}Tl, as described in this thesis.

In this data analysis, 88 new transitions were established with a precise determination of their energies, relative intensities, and DCO ratios. This led to the development of a new level scheme that has extended earlier versions significantly, up to spins of $\frac{45}{2}^+$ and $\frac{37}{2}^-$, respectively, in the two main branches. In the new level scheme the presence of two strongly coupled, oblate rotational bands (Bands 1 and 2) is most significant. One is of negative parity and built on the $\pi h_{9/2}$ orbital, the other one is of positive parity and built on the $\pi i_{13/2}$ orbital. Both of these bands extend from low to high spin through the region of a $(\nu i_{13/2})^2$ backbend. This allows a study of their crossing frequencies. In addition, a relatively low-lying level structure (Band 3) has been explored; it is clearly of non-rotational character. No evidence has been found in the data for a normally deformed prolate band built on either $\pi h_{9/2}$ or $\pi i_{13/2}$ orbitals.

All of this culminates in a shape coexistence picture. Three different shapes are present in ^{191}Tl: oblate, spherical, and superdeformed prolate. Whereas the $h_{9/2}$ rotational band corresponding to a slightly oblate shape was discovered in ^{191}Tl and neighboring isotopes some time ago, the existence of an oblate $\pi i_{13/2}$ band is established for the first time. It is also interesting to see that a spherical structure is present and competitive at moderate spin. The presence of superdeformed bands illustrates the variety of shapes in this nuclear mass region and is an important test for the model predictions used in this work.

For a detailed description of the two oblate band structures, TRS calculations were examined. These define a stable deformed minimum with a deformation $\beta_2 \approx 0.15$ around the oblate-collective axis ($\gamma = -60°$) for negative-parity configurations. For positive parity configurations the Fermi surfaces are more complicated. A shallow nearly oblate local minimum with $\beta_2 \approx 0.19$ is present as well as a nearly spherical one. However, this situation is consistent with the more complex and complicated level structures in the positive parity branch of the scheme. It appears that nearly oblate and nearly spherical shapes are very competitive up to relatively high spins.

The study of $\nu i_{13/2}$ crossing frequencies, $\hbar\omega_c$, shows some agreement and some disagreement with the predictions of theory. The crossing frequency in the $\pi h_{9/2}$ band is higher than that in the $\pi i_{13/2}$ band, both in ^{191}Tl and in ^{193}Tl [11]. This agrees with the TRS prediction that the former configuration has a smaller deformation that the latter. However, there is a problem in comparing the Tl crossing frequencies with those of the core. The ^{190}Hg core, which has the lowest β_2 value (from TRS), also has the lowest experimental $\hbar\omega_c$. Perhaps this discrepancy is due to the fact that other shape parameters (*e.g.* γ) need to be considered more carefully in the Cranked Shell Model Calculations.

For the non-rotational levels of band structures 3 and 3a a tentative explanation is offered: they are related to coupling ${h_{9/2}}^-$ and ${i_{13/2}}^+$ configurations to spherical states in the neighboring nucleus ^{192}Pb. This coupling scheme serves quite well in describing the observed level spins. It also explains that the tentatively assigned parities of Bands 3 and 3a have opposite signs. Possibly, a prolate non-collective energy minimum ($\gamma = 120°$) is involved in the underlying nuclear structure.

5.2 Future Directions

The work presented herein might also be a starting point for continuing studies on ^{191}Tl and neighboring isotopes. Besides nuclear structure research in the superdeformed well, the following questions are important for the understanding of these nuclei:

Continuation of the regular $\pi i_{13/2}$ band structure above the backbending. Establishing $E2$ behaviors between higher-lying states is important. In particular, if $M1/E2$ mixing ratios could be obtained for this part of the newly established band, it would be possible to obtain new information on the sign of the deformation parameter γ. In the present data, the $E2$ transitions above the band crossing are too weak to be observed.

Observation of prolate band structures with moderate deformation. The possibility of a prolate band built on either the $\pi h_{9/2}$ or $\pi i_{13/2}$ orbital was discussed in the introduction. In the isotones ^{187}Tl [7] and ^{186}Hg [37], for example, such prolate bands are seen. Their bandhead energies should rise significantly when going to higher neutron numbers, see Fig. 1.3. Consequently, such a band, if present, should be weakly populated. This is most likely the reason why there is no evidence in the present data for a prolate structure in ^{191}Tl (besides the superdeformed bands). If it is observed, this would be the first case for coexistence of four different shapes (oblate, spherical, prolate, and superdeformed) in the same nucleus.

To become more sensitive for these γ-ray sequences most probably embedded in a relatively large background, more powerful detection systems are necessary. Very recently, these have become available: the Gammasphere at the Lawrence Berkeley Laboratory in California and the Eurogam device located at CRN in Strasbourg, France. The Gammasphere presently consists of 36 CSGs, only a third of the 4π arrangement planned for the final version (for the end of 1994). Due to a high probability for three and higher-fold coincidences, the experimenter will gain two or three orders of magnitude in the ability to isolate a spectrum from background compared to previous devices. Recently, new data on ^{192}Tl and ^{191}Tl have been taken at Gammasphere by a collaboration of the Argonne group and our group. The analysis of these high-statistic, multi-gamma coincidence measurements should enable one to make further comment on the questions left unanswered in this work.

BIBLIOGRAPHY

Bibliography

[1] A. Kahler, Ph.D. dissertation, University of Tennessee, 1978.

[2] L. Goettig, *et al.*, in *Annual Report, Nuclear Structure Laboratory* (unpublished), page 85, University of Notre Dame (1987).

[3] E. Coenen *et al.*, *Phys. Rev. Lett.* **54** 1783 (1985).

[4] R.M. Diamond and F.S. Stephens, *Nucl. Phys.* **45** 632 (1963).

[5] J.O. Newton *et al.*, *Nucl. Phys.* **A236** 225 (1974).

[6] H. Huebel *et al.*, *Nucl. Phys.* **A453** 316 (1986).

[7] W. Reviol *et al.*, *Phys. Rev.* **C49** R587 (1994).

[8] R.V.F Jansens *et al.*, *Phys. Lett.* **B131** 35 (1983).

[9] H. Sergolle *et al.*, *Z. Phys.,* **A313** 289 (1983).

[10] Porquette *et al.*, *Phys. Rev.* **C44** 2445 (1991).

[11] W. Reviol *et al.*, *Nucl. Phys.* **A548** 331 (1992).

[12] z. Chunmei, *Nuclear Data Sheets* **57** 25 (1989).

[13] S. Pilotte *et al.*, *Phys. Rev.* **49** 718 (1994).

[14] G.F. Knoll, Radiation Detection and Measurement. John Wiley and Sons (1989)

[15] N.R. Johnson *et al.*, *ORNL-6233* p 158 (1985).

[16] The Harshaw Chemical Co., App Note (1980)

[17] T.K. Alexander and J.S Forster, *Adv. Nucl. Phys.* **Vol 10** 197 (1979).

[18] M. Jaaskelainen, *Nucl. Inst. and Meth.* **204** 385 (1983).

[19] ORNL-Holifield Users Handbook.

[20] C. Lederer and V. Shirley, Tables of Isotopes, Seventh Edition, Appendix II.

[21] D. C. Radford *et al.*, *Nucl. Inst. and Meth.* **A258** 111 (1987).

[22] Computer code GF2, obtained from D.C. Radford, AECL Chalk River, Chalk River, Ontario, Canada.

[23] F. Roesel *et al.*, *Atomic Data and Nuclear Data Tables* **21** 368 (1978).

[24] R.M. Steffen and K. Alder, in: The Electromagnetic interaction in Nuclear Spectroscopy, edited by W.D. Hamilton (North Holland 1975) 505.

[25] K.S. Krane *et al.*, *Atomic Data and Nuclear Data Tables* **11** 351 (1973).

[26] A. Kraemer-Flecken *et al.*, *Nucl. Inst. and Meth.* **A275** 333 (1989).

[27] M.W. Drigert *et al.*, *Nucl. Phys.* **A515** 466 (1990).

[28] S. Raman *et al.*, *Atomic Data and Nuclear Data tables* **36** 20 (87).

[29] R. Holtzman, *Nucl. Inst. and Meth.* **A260** 153 (1987).

[30] S. Cwiok *et al.*, *Comput. Phys. Commun.* **46** 379 (1987).

[31] W. Nazarewicz *et al.*, *Nucl. Phys.* **A435** 397 (1985).

[32] J. Dudek, Int. Winter Meeting on Nuclear Physics, Bormio, Italy, 1987. Ed. I. Iori, Ricerca Scientifica ed Educzione Permanente, Milano 1987.

[33] R. Wyss, *Nucl. Phys.* **A511** 324 (1990).

[34] A. Anderson *et al.*, *Nucl. Phys.* **A268** 205 (1976).

[35] A. Plompen *et al.*, *Nucl. Phys.* **A562** 61 (1993).

[36] S.M. Harris, *Phys. Rev.* **B138** 509 (1965).

[37] W.C. Ma *et al.*, *Phys. Rev.* **C47** R5 (1993).

[38] M. Goldhaber, *Phys. Rev.* **C17** 1171 (1978).

VITA

John Lewis was born in Johnson City, Tennessee, on May 29, 1966. He grew up there and attended Oak Street Baptist Church, which he still considers as his home church. John attended the Happy Valley schools for all grades K–12 and graduated from there as co-valedictorian in the spring of 1984. The following fall, he entered King College in Bristol, Tennessee as an undergraduate. Graduating from this institution in the spring of 1988, he received a Bachelor of Science degree in both Physics and Mathematics. After this, he entered the University of Tennessee, Knoxville as a teaching assistant for the undergraduate physics laboratory. After his first year of graduate studies, he joined the Nuclear Physics Research Group as a Research Assistant and began work toward the Master of Science degree in Physics.